Analysis of the flow and mass transfer processes for the incompressible flow past an open cavity with a laminar and a fully turbulent incoming boundary layer

By KYOUNGSIK CHANG[1], GEORGE CONSTANTINESCU[2]† AND SEUNG-O PARK[1]

[1]Korean Advanced Institute of Science and Technology, 373-1 Kusong-dong, Yusong-gu, Daejeon 305-701, Korea

[2]Civil and Environmental Engineering, The University of Iowa, IIHR – Hydroscience and Engineering, M. Stanley Hydraulics Laboratory, Iowa City, IA 52242-1585, USA

The three-dimensional incompressible flow past a rectangular two-dimensional shallow cavity in a channel is investigated using large-eddy simulation (LES). The aspect ratio (length/depth) of the cavity is $L/D = 2$ and the Reynolds number defined with the cavity depth and the mean velocity in the upstream channel is 3360. The sensitivity of the flow around the cavity to the characteristics of the upstream flow is studied by considering two extreme cases: a developing laminar boundary layer upstream of the cavity and when the upstream flow is fully turbulent. The two simulations are compared in terms of the mean statistics and temporal physics of the flow, including the dynamics of the coherent structures in the region surrounding the cavity. For the laminar inflow case it is found that the flow becomes unstable but remains laminar as it is convected over the cavity. Due to the three-dimensional flow instabilities and the interaction of the jet-like flow inside the recirculation region with the separated shear layer, the spanwise vortices that are shed regularly from the leading cavity edge are disturbed in the spanwise direction and, as they approach the trailing-edge corner, break into an array of hairpin-like vortices that is convected downstream the cavity close to the channel bottom. In the fully turbulent inflow case in which the momentum thickness of the incoming boundary layer is much larger compared to the laminar inflow case, the jittering of the shear layer on top of the cavity by the incoming near-wall coherent structures strongly influences the formation and convection of the eddies inside the separated shear layer. The mass exchange between the cavity and the main channel is investigated by considering the ejection of a passive scalar that is introduced instantaneously inside the cavity. As expected, it is found that the ejection is faster when the incoming flow is turbulent due to the interaction between the turbulent eddies convected from upstream of the cavity with the separated shear layer and also to the increased diffusion induced by the broader range of scales that populate the cavity. In the turbulent case it is shown that the eddies convected from upstream of the cavity can play an important role in accelerating the extraction of high-concentration fluid from inside the cavity. For both laminar and turbulent inflow cases it is shown that the scalar ejection can be described using simple dead-zone theory models in which a single-valued global mass

† Author to whom correspondence should be addressed: sconstan@engineering.uiowa.edu

exchange coefficient can be used to describe the scalar mass decay inside cavity over the whole ejection process.

---

1. Background

Cavity flows are encountered in many engineering applications, for example in the bomb bay and landing systems of aircraft, in the sunroof on cars or in flow over ground vehicles. In these flows the incoming boundary layer at the leading edge of the cavity may be laminar or turbulent. The effect of pressure and velocity oscillations induced by the eddies generated in the shear layer on top of the cavity is to generate aero-acoustic noise and vibrations that can eventually increase the fatigue of these structures. For environmental applications, the presence of cavity-like geometries in rivers, lakes or urban canyons, especially under stratified conditions, is of interest because of the transport processes (toxic air, pollutants, nutrients, suspended sediments, aerosol, etc.) that occur between the cavity and the main flow current. Thus the quantitative characterization of the mass exchange between the cavity and the surrounding is highly important. Pollutant, denser water or toxic air may accumulate in these cavities and produce a stagnant pool which may be harmful to the environment. For instance, if the ejection of the pollutant or stagnant water inside cavity-like regions in rivers is too slow, fish that generally use these low-velocity regions for shelter from predators or environmental stressors (e.g. pollution), feeding and reproduction purposes would have to avoid them. Another environmental application is related to the release of chemical toxic substances into an urban canyon whose shape resembles in many cases that of a cavity. In the case of the purging of a pollutant or other hazardous substance that accumulates or was dumped intentionally or accidentally into a cavity, accurate prediction of the travel time, maximum concentration and spreading of the pollutant cloud requires accurate quantification of the exchange processes between the main channel and the cavity region. In all these examples the flow upstream of the cavity is generally fully turbulent and incompressible.

The main feature of low-Mach-number cavity flows in what is called the shear layer mode (which is investigated in the present numerical study) is the presence of a complex mechanism which consists of the generation of vortices at the leading edge of the cavity due to Kelvin–Helmholtz instabilities, followed by their convection and impingement on the trailing-edge. This leads to injection of patches of vorticity inside the cavity in an unsteady fashion. Strong fluctuations develop at the trailing-edge corner due to its interaction with these patches of vorticity. These interactions are expected to be quasi-regular in the case of an incoming laminar boundary layer and fairly random for a highly turbulent incoming flow especially if the incoming boundary layer thickness is large. As discussed by Lin & Rockwell (2001), the possible forcing of the separated shear layer by the unsteady recirculating flow within the cavity may affect the overall growth and energy amplification in the shear layer as well as the growth of secondary instabilities that are responsible for the spanwise three-dimensionality of the separated shear layer. Rockwell & Knisely (1980) studied experimentally the spanwise structure of the separated shear layer and observed a secondary longitudinal instability that acts on the primary instability associated with the growth of the spanwise oriented vortex tubes. In these flows, it was observed that the form and strength of the pressure and velocity oscillations are strongly dependent

on the cavity geometry (length to depth ratio) and the flow conditions (Reynolds number, incoming boundary layer characteristics, etc.).

For quasi-incompressible flows, Sarohia (1977) studied experimentally the flow around an axisymmetric cavity and measured the minimum cavity length for oscillations to occur over the cavity. He focused on the study of the variation of velocity fluctuations along the shear layer on top of the cavity and found that the oscillations jumped to a higher (frequency) mode as the length was increased. Rockwell (1977) and Rockwell & Naudasher (1978) predicted the main oscillatory frequency for incompressible flow over two-dimensional cavities based on linear inviscid stability theory (laminar conditions at separation). The predictions agreed well with the experimental data of Ethembabaoglu (1973). Knisely & Rockwell (1982) studied the streamwise amplification of the shear layer oscillations and their spectral content for the flow over a rectangular cavity in the shear layer mode. They showed that besides the fundamental oscillatory frequency, a number of additional, primarily lower frequency, oscillations can exist. The energy associated with these modes can be comparable to that of the fundamental oscillatory frequency. Neary & Stephanoff (1987) studied the shear layer properties of the flow in a shallow cavity (length over depth ratio $L/D = 3.5$) with a laminar boundary layer upstream of the cavity. Pereira & Sousa (1994, 1995) studied the incompressible flow past a rectangular cavity with turbulent upstream conditions at a moderate Reynolds number ($Re_D = 3360$), in particular the influence of the trailing-edge geometry on the flow inside the separated shear layer and cavity. Lin & Rockwell (2001) used particle image velocimetry (PIV) techniques to study the flow over a two-dimensional cavity ($Re_D \sim 27\,800$) with a turbulent boundary layer inflow (momentum thickness was $\theta \sim 0.049D$). They found that the large-scale eddies in the separated shear layer scale with the mean momentum thickness of the boundary layer at separation. The frequency of their formation was close to the one predicted by inviscid theory. They attributed the presence of smaller eddies that oscillate at higher frequencies inside the shear layer to the incoming flow structures that are present in the approach turbulent boundary layer. Cross-wire anemometer and laser Doppler velocimetry (LDV) measurements of the flow field within a shallow cavity ($L/D = 4$) were recently performed by Grace, Dewar & Wroblewski (2004) for the case of both a laminar and a turbulent incoming boundary layer ($Re_D = 12\,500$ and $Re_D = 24\,800$). In both cases measurements of the velocity spectra in the separated shear layer did not predict any peaks that would correspond to the quasi-regular formation of large-scale eddies in the separated shear layer, suggesting that the cavity was in the non-resonating regime in contrast to Lin & Rockwell's results. The detailed LDV measurements showed that the distribution of the Reynolds shear stress was strongly dependent on the upstream flow conditions.

Most numerical investigations of cavity flows, especially the ones in which eddy resolving techniques like direct numerical simulation (DNS) or large-eddy simulation (LES) were used, have focused on the compressible case (both subsonic and supersonic regimes) with a developing laminar or, in the case of LES, relatively thin turbulent incoming boundary layer. Among recent DNS studies are the two-dimensional DNS investigations of Rowley, Colonius & Basu (2002) who investigated the subsonic flow (Mach number, $Ma = 0.2-0.8$) over two-dimensional cavities of different aspect ratios with laminar inflow conditions ($Re_D = 1500$). The investigation focused on the differences between the flow past cavities in the shear layer mode and in the wake mode, as well as on the transition between them. Shieh & Morris (2001) performed three-dimensional Reynolds-averaged Navier–Stokes (RANS) and detached eddy simulation (DES) calculations of the flow over two-dimensional and

three-dimensional cavities at $Ma = 0.6$ and $Re_D = 2 \times 10^5$. A turbulent boundary layer profile was specified upstream of the cavity. The wake mode was found to be present in the simulations of the two-dimensional cavities, and the shear mode in their simulations of flow past three-dimensional cavities. Gloerfelt *et al.* (2002) performed three-dimensional DNS simulations at $Ma = 0.6 - 0.8$ for two-dimensional cavities with a laminar inflow boundary layer on fine meshes ($\sim 5.4 \times 10^6$ cells). They also used three-dimensional LES to study the case in which a turbulent incoming boundary layer was present. Larchevêque *et al.* (2003) performed LES of subsonic ($Ma = 0.8$) flow over a deep cavity ($L/D = 0.42$) at a Reynolds number, defined with the length of the cavity, of 860 000 using both a mixed subgrid-scale model in which case a mixed two-dimensional/three-dimensional method was used and a monotonically integrated large-eddy simulation (MILES) scheme in which case full three-dimensional simulations were performed. Wall functions were used, and the mesh sizes were in the range of 0.7×10^6 to 1.7×10^6 cells. Overall, they found good agreement with the experimental data of Forestier, Jacquin & Geffroy (2003). The same group (Larchevêque *et al.* 2004) performed simulations of the flow over a shallow cavity ($L/D = 5.0$) at $Re = 7 \times 10^6$ and $Ma = 0.85$ on a mesh with 6×10^6 cells and demonstrated that the upstream part of the separated shear layer is dominated by the Kelvin–Helmholtz instability that appears to be forced near the origin of the layer, while the downstream zone behaves similarly to a free mixing layer over which spreading is linear. They used spectral analysis to investigate in detail the dynamics of the coherent structures and the characteristics of the Rossiter modes.

For incompressible cavities, Pereira & Sousa (1995) used two-dimensional DNS to study the coupling between the shear layer and the recirculating flow in a two-dimensional cavity. Yao, Cooper & Raghunthan (2001) used LES with a dynamic subgrid-scale model to calculate the flow past a three-dimensional cavity ($L/D = 4.0$, $W/L = 3.0$, where W is the width of the cavity). A laminar Blasius profile was assumed at the inlet. The authors are not aware of any three-dimensional LES or DNS of the incompressible flow over a cavity for the case in which the incoming flow is fully turbulent.

The objectives of the present paper are to use highly resolved simulations to: (i) examine three-dimensional flow features of incompressible cavity flows with a laminar boundary layer and fully turbulent flow upstream of the cavity, in particular the changes in the shear layer structure between the two regimes; (ii) investigate the influence of the recirculating flow inside the cavity on the separated shear layer; (iii) study the nature of the interactions between the large-scale eddies and the trailing-edge corner; (iv) study the amplification of the instabilities and/or turbulence in the shear layer on the top of the cavity; (v) investigate the effect of the near-wall coherent structures that are present in the approach channel on the dynamics of eddies inside the separated shear layer and ultimately on the nature of the interactions between these eddies and the trailing-edge corner for the case in which the incoming flow is fully turbulent; (vi) investigate the mass exchange processes between the cavity and the channel by studying the ejection of a passive scalar introduced instantaneously inside the cavity; (vii) quantify the acceleration of the purging process in the case in which the flow upstream of the cavity is fully turbulent.

2. Numerical method

In the present work, a non-dissipative massively parallel finite-volume DNS/LES code developed by Pierce & Moin (2001) is employed. The code solves the conservative form of the incompressible Navier–Stokes equations on non-uniform Cartesian
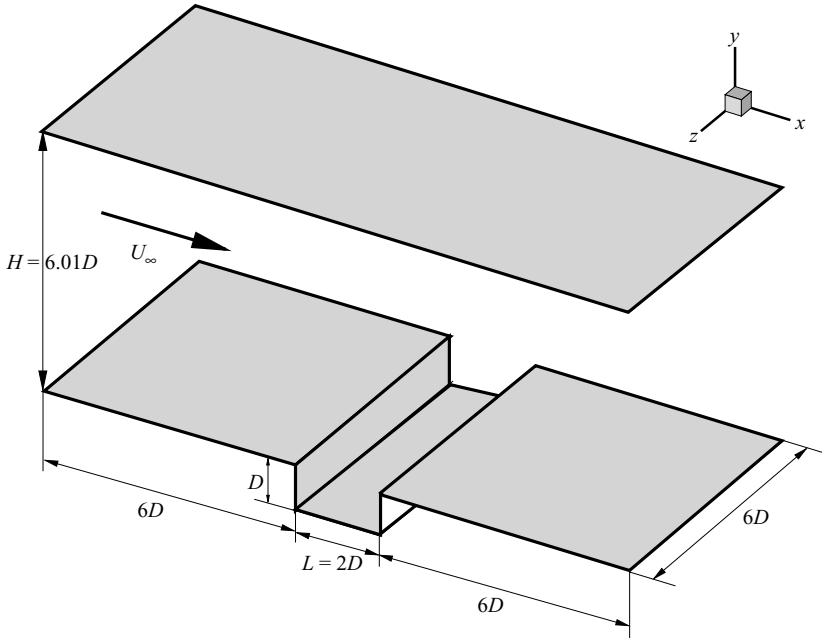
FIGURE 1. Computational domain.

meshes. The Pressure Poisson algorithm uses a staggered conservative space–time discretization with a semi-implicit iterative method to advance the equations in time such that the algorithm is second-order accurate in space and time. The numerical method discretely conserves energy. This ensures robustness at relatively high Reynolds numbers while using strictly non-dissipative (central) discretizations to solve for the momentum and pressure. The scalar transport is modelled using an advection–diffusion equation in which the convective terms are discretized using QUICK scheme to alleviate the problems associated with the formation of wiggles in the scalar fields. For LES, the subgrid-scale viscosity and diffusivity coefficients are calculated dynamically (Pierce & Moin 2001). The viscous Schmidt number Sc was taken equal to 1. No assumptions are needed on the value of the turbulent Schmidt number as the dynamic procedure estimates directly, based on the resolved velocity and concentration fields, the value of the eddy diffusivity. The code was parallelized using MPI. Details on the numerical method and code validation for non-reacting and reacting flow simulations are available in Pierce & Moin (2001).

3. Simulations overview

The computational domain considered in the present work is similar to that in the water tunnel experiments of Pereira & Sousa (1994, 1995) for which the upstream flow was turbulent. The aspect ratio (length/depth) of the shallow cavity is $L/D = 2$ and the Reynolds number Re_D defined with the cavity depth (D) and the mean velocity in the upstream channel (U) is 3360. The Reynolds number defined with the upstream channel height is $Re_H = 20\,450$. Figure 1 shows the overall geometry and computational domain. The length of the computational domain in the spanwise direction is equal to $6D$. The flow in the simulations is considered to be periodic in the spanwise direction (two-dimensional cavity). The mesh size is close to 14 million cells ($320 \times 224 \times 192$ in the streamwise, vertical and spanwise directions). The first

	Re_D	δ/D	δ^*/D	θ/δ	H	θ/L	L/θ	Re_δ
Laminar	3360	0.18	0.07	0.160	2.50	0.0144	69.5	604
Turbulent	3360	2.50	0.43	0.110	1.55	0.134	7.2	8400
Experiment	3360	2.48	–	0.097	–	0.121	8.3	8382

TABLE 1. Boundary layer parameters for the present simulations and experiment of Pereira & Sousa (1995).

point away from the solid surfaces is located at about 0.15 wall units (assuming turbulent flow and a mean friction velocity of $u_\tau/U \sim 0.05$); the characteristic cell size in the cavity region is close to 6 wall units. In the spanwise direction the grid spacing is about 5 wall units which is sufficient to accurately resolve the low- and high-speed streaks in the near-wall region. The resolution in the cavity region for the turbulent inflow case is comparable to DNS requirements. All the walls were treated as no-slip surfaces and no wall functions were used. At the outflow a convective boundary condition was used. A statistically steady solution was obtained after about $50D/U$ after which statistics were collected over $100D/U$. The sensitivity of the flow to the characteristics of the upstream flow is studied by considering two extreme cases. In the first case the velocity profile immediately upstream of the cavity corresponds to a developing laminar boundary layer, while in the second case the flow is fully turbulent.

In the laminar inflow case (LC) the flow in the inlet section is uniform and no fluctuations are added in time. The solution is jittered at the start of the simulation to allow instabilities to develop. At the leading cavity edge the thickness of the developing boundary layer (Blasius profile) is $\delta/D = 0.18$. The other characteristics of the boundary layer at separation, including the displacement thickness δ^*, momentum thickness θ and the shape factor H, are indicated in table 1. The flow is observed to remain laminar over the cavity and immediately downstream of it. This is not a consequence of the subgrid-scale viscosity introduced by the LES model. The dynamic model was found to predict very low values of the subgrid-scale viscosity compared with the molecular viscosity over practically the whole domain. This is expected to happen in a simulation using a dynamic LES model in regions in which the flow remains laminar.

In the fully turbulent inflow case (TC), the instantaneous velocity components at the inflow section were obtained from a preliminary simulation of the flow in a straight channel of identical section to the one which contains the cavity on its bottom wall. In this simulation the flow was assumed periodic in the streamwise direction and the channel Reynolds number was identical to the corresponding one in the full simulation that included the cavity ($Re_H = 20\,450$). The instantaneous velocity fields were then fed in a time accurate way through the inlet section during the simulation of the flow past the cavity. In this way the incoming flow contains the expected near-wall coherent structures including the wall streaks that are accurately resolved in both the preliminary channel simulation and the cavity simulation. Table 1 contains the parameters characterizing the incoming turbulent boundary layer at the cavity leading edge corresponding to the fully turbulent inflow simulation and the experiment (Pereira & Sousa 1994, 1995). The measured turbulence intensity at the channel centreline upstream of the cavity was 4 % in the experiment and about 3.6 % in the LES.

The mass exchange between the cavity and the main channel is investigated by considering the ejection of a passive scalar that is introduced instantaneously at a certain time (after the velocity fields become statistically steady) inside the cavity
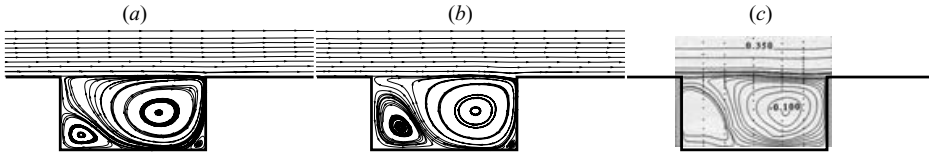
FIGURE 2. Mean flow streamlines: (*a*) laminar; (*b*) turbulent; (*c*) experiment of Pereira & Sousa (1994).
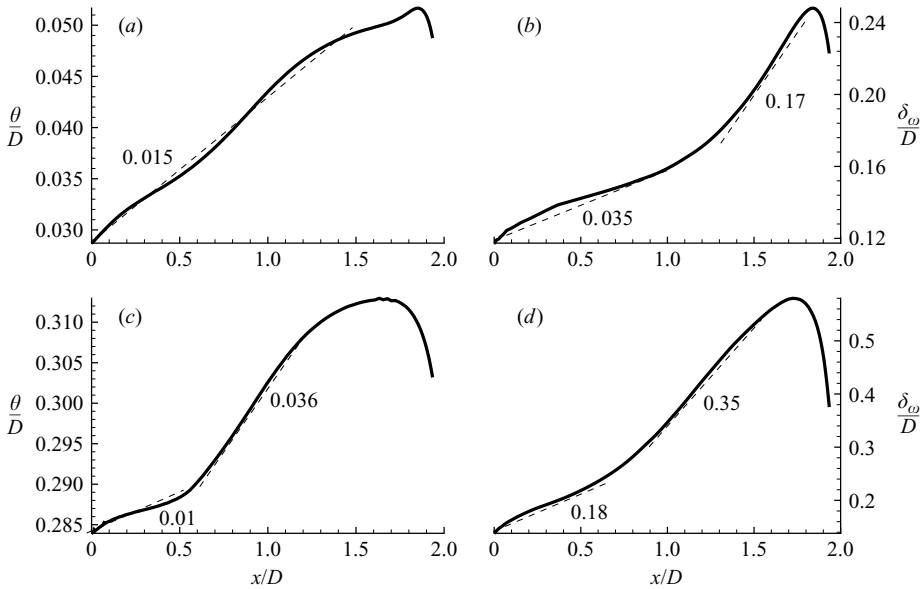

FIGURE 3. Momentum and shear layer (vorticity) thickness over the cavity, with mean slope as shown by dashed lines: (*a*) θ laminar; (*b*) δ_ω laminar; (*c*) θ turbulent; (*b*) δ_ω turbulent.

domain ($2D \times 1D \times 6D$). The non-dimensional scalar concentration C is initialized as $C = 1$ inside the cavity and $C = 0$ outside it at the time at which the mass exchange process between the channel and the cavity starts. This time is formally taken as $t = 0D/U$.

4. Results and discussion

4.1. *Mean quantities and flow statistics*

Figure 2 shows the mean streamlines corresponding to the two simulations along with the ones determined from the experiment. Two large recirculation eddies are observed in both simulations, though in the TC the main downstream recirculation eddy is smaller compared to the LC. The size and relative position of the two main eddies inside the cavity for the TC are very similar to the corresponding (sharp trailing-edge corner experiment) mean flow streamlines visualizations of Pereira & Sousa (1994). In particular, the simulation (compare figures 2*b* and 2*c*) captures very well the elongated shape of the main recirculation eddy in the upper upstream region of the cavity.

The shear layer on top of the cavity is expected to differ from a mixing layer mainly due to the effect of the cavity flow below that can modify the entrainment rate. The momentum thickness (θ) and the vorticity shear layer thickness (δ_ω) variation over the cavity are plotted in figure 3. Though normally the momentum thickness is used

to characterize the shear layer thickness growth, because of the presence of the cavity and the associated recirculation region, there is some ambiguity in defining it for the case of the flow over cavity. The vorticity thickness which is a measure of the maximum local shear is defined in a non-ambiguous way.

In the LC ($L/\theta = 69.5$) the spreading rate varies between 0.035 ($x/D < 1$) and 0.17 ($1.4 < x/D < 1.7$). For $x/D > 1.7$ the blocking effect due to the presence of the trailing-edge induces a sharp decay in the spreading rate. The averaged rate of $d\delta_\omega/dx$ ($x < 1.7$) is 0.07 which is close to those obtained by Rowley *et al.* (2002) in their two-dimensional DNS compressible flow simulations with an incoming laminar boundary layer. The mean spreading rates in their simulations were 0.05 for $L/\theta = 59$ and 0.07 for $L/\theta = 90$. The values obtained by Sarohia (1977) for similar conditions were 0.056 and 0.064. The main difference with Sarohia's results is the rather sharp increase in the spreading rate around $x/D = 1$. This is because for our conditions (no fluctuations added at the inflow) the separated shear layer starts shedding relatively late, at around $x/D = 1$ (see also discussion of figure 8). When the shedding of the quasi-two-dimensional spanwise vortices starts, the growth of the shear layer thickness should be larger. A secondary effect that contributes to this accelerated growth is the fact that the growth of the three-dimensional instabilities over the second half of the cavity length is larger (e.g. formation of the hairpin vortices as a result of the interactions with the trailing-edge corner) and the downstream part of the cavity contains more three-dimensional structures. Interestingly, the spreading rate of the momentum thickness is relatively constant at around 0.015 ($0 < x/D < 1.6$) which is within the range measured by Sarohia (1977) for laminar thin incoming boundary layers with similar values of L/θ at $x/D = 0$ and in which the second mode of oscillation was observed in experiments.

As expected the growth rate of δ_ω is higher in the TC. The spreading rate is close to 0.18 for $x/D < 0.7$ and then is practically constant at 0.35 for $1 < x/D < 1.7$. The value of $d\delta_\omega/dx$ over the upstream part of the cavity ($x/D = 0.7$) is very close to that measured by Brown & Roshko for a turbulent free shear layer (0.162). As shown later (e.g. see discussion of figure 16) the near-wall structures convected from upstream of the cavity strongly disturb from above the vorticity sheet associated with the separated shear layer. As a result of these interactions, for $x/D > 0.7$ patches of isolated vorticity are forming and are then convected toward the trailing-edge corner (see discussion of figures 9 and 11). Instantaneous visualizations of the evolution of these three-dimensional eddies show that merging occurs frequently, pointing to the strong nonlinear interactions among these eddies as a possible mechanism responsible for the higher growth rates for $x/D > 0.7$. A secondary effect that is taking place around $x/D = 0.8 - 1$ is the forcing due to the modulations in the intensity of the jet-like flow inside the cavity. Due to the interactions with the trailing-edge corner, patches of vorticity are entrained inside cavity and then recirculated. As they approach the top of the cavity they further jitter from below the structures present in the downstream part of the shear layer on top of the cavity and contribute to the overall growth of the shear layer over this region. The momentum thickness growth rate is around 0.01 for $x/D < 0.7$ and close to 0.036 for $1 < x/D < 1.7$ which is within the typical range (0.03–0.04) expected for turbulent incoming boundary layers (Gloerfelt *et al.* 2002; Larcheveque *et al.* 2003, 2004; Forestier *et al.* 2003). Note that the range of 0.03–0.04 corresponds to thin incoming boundary layers ($L/\theta > 60$) while in our case $L/\theta \sim 8$. The reasons for the change in the growth rate of θ are same as the ones given for δ_ω. The variation of $d\theta/dx$ over the cavity is different to that observed for an incoming thin turbulent boundary layer by Larcheveque
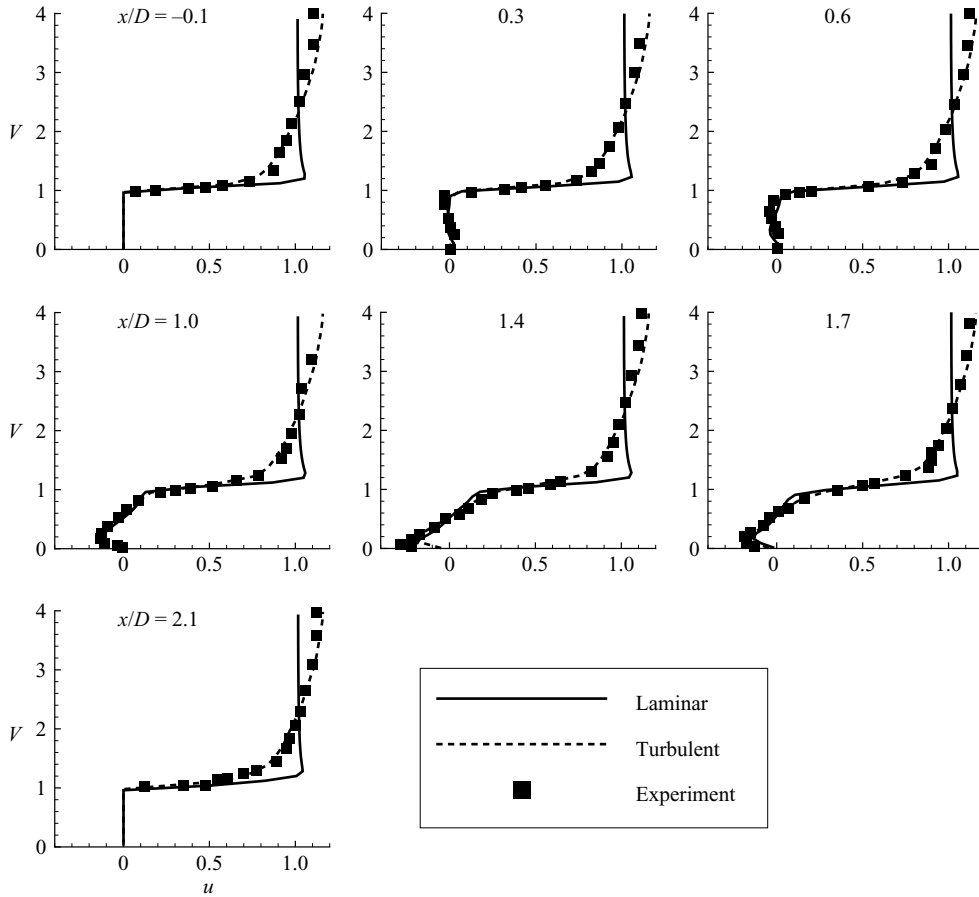
FIGURE 4. Mean streamwise velocity profiles at different streamwise stations. Symbols correspond to the experiment of Pereira & Sousa (1995).

et al. (2003). In their simulation a region of large spreading rates was identified over the upstream part of the cavity. The main reasons identified by the authors were the pairing of quasi-two-dimensional vortices observed to occur over the initial region on top of the cavity and the subharmonic forcing by pressure waves. In our TC case (figures 8 and 16) no quasi-two-dimensional vortices are present in the separated shear layer.

The comparison of the longitudinal mean velocity profile with the experimental data of Pereira & Sousa (1995) is shown in figure 4 at seven stations from $x/D = -0.1$ to $x/D = 2.1$. A very good agreement is observed at all stations between the experimental data and the TC predictions. In the LC the profiles show clear differences with the experiment, especially across the shear layer and above it, but this is expected as in the experiment the flow upstream of the cavity was turbulent. In the LC the decay of vorticity inside the separated shear layer is much sharper on the side toward the channel and the streamwise decay of vorticity is much milder than in the TC. This explains the very abrupt streamwise velocity variation across the shear layer observed at all streamwise stations.

Profiles of the resolved normal stresses in all three directions and of the shear stress $\overline{u'v'}$ at different streamwise locations starting just upstream of the cavity ($x/D = -0.1$)
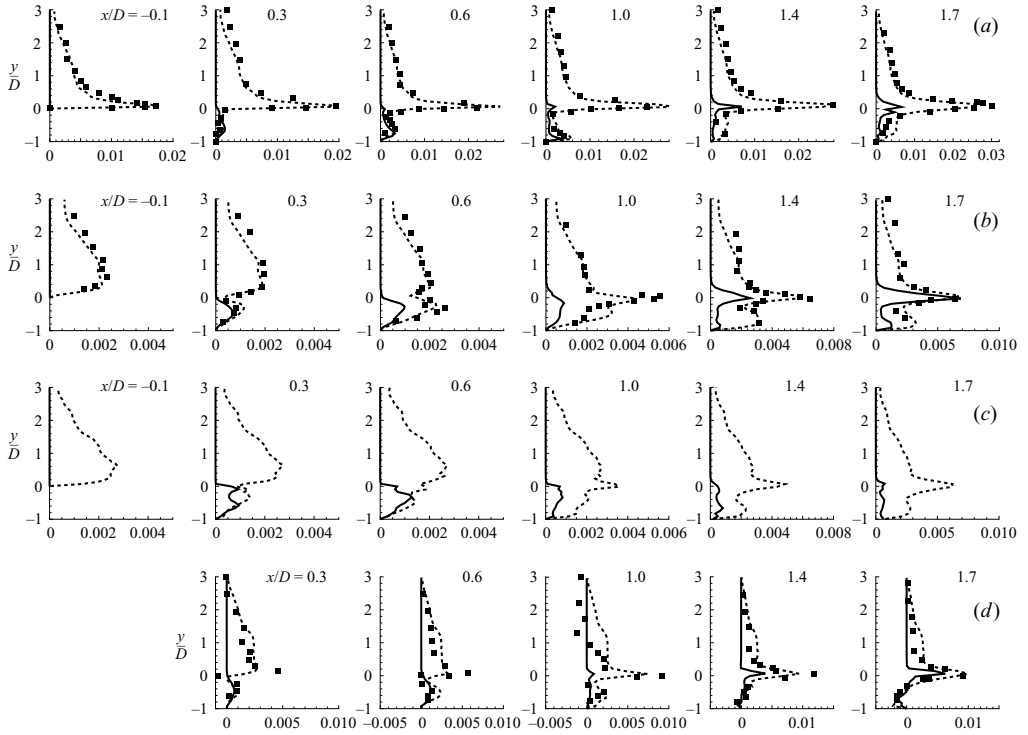
FIGURE 5. Resolved stresses for laminar (solid line) and turbulent (dashed line) inflow cases at different streamwise stations. Symbols correspond to experimental measurements of Pereira & Sousa (1994). (a) $\overline{u'u'}$; (b) $\overline{v'v'}$; (c) $\overline{w'w'}$; (d) $\overline{u'v'}$.

and continuing until $x/D = 1.7$, close to the cavity trailing-edge ($x/D = 2$) are shown in figure 5 for the two simulations along with the experimental measurements of Pereira & Sousa (1994). All the stresses are non-dimensionalized by the mean velocity at the channel centreline upstream of the cavity (in the laminar case the value is equal to the bulk velocity U). For the LC the stresses correspond to the apparent stress induced by the laminar instabilities and the convection of coherent structures present in the separated shear layer and cavity regions. As the flow upstream of the cavity is steady, the averaging process generates relatively high values only in the downstream half of the shear layer and then inside the cavity and near the bottom of the channel, downstream of the cavity. In the TC the resolved stress is a consequence of the turbulence (small scales) and organized (large scales) motions. Though relatively large streamwise fluctuations are observed in the incoming turbulent boundary layer (the largest values are observed around a plane situated $0.09D$ from the channel bottom), there is a significant intensification of these fluctuations inside the separated shear layer. In the case of the spanwise and vertical fluctuations, the amplification is present but takes place mostly over the downstream half of the detached shear layer and in the downward jet-like flow close to the trailing-edge. Overall the vertical and spanwise fluctuations are significantly lower than the streamwise ones.

The results corresponding to the TC are in good overall agreement with the experimental data. For instance, the predicted distributions of $\overline{u'u'}$ accurately capture the peak values at practically all sections and the rates of decay across the separated shear layer. As observed in figure 5(a), the decay is relatively mild toward the

channel side. On the cavity side the TC simulation captures the secondary peak in the streamwise normal stress at $x/D = 0.6$ and $x/D = 1.0$ associated with the detachment of the wall-jet-like current from the cavity bottom. Some disagreement between simulation and experiment is however observed in the profile at $x/D = 1.7$ in the region corresponding to the middle of the cavity. In the LC the flow at the cavity leading edge is steady and flow remains laminar over the cavity. This explains the fact that $\overline{u'u'}$ is equal to zero at $x/D = -0.1$. Over the upstream part of the cavity the shear layer starts oscillating but does not shed, thus the small peak value recorded near $y/D = 0.0$ at $x/D = 0.6$. Some larger values are recorded inside the cavity. They are due to the quasi-periodic convection of patches of vorticity inside the cavity (see also discussion of figure 10) followed by separation of the jet-like current similar to the TC.

The vertical normal stress $\overline{v'v'}$ distribution (figure 5b) in the TC is also in close agreement with the experiment with the exception of stations $x/D = 0.3$ and 1.4 where on the channel side for $y/D > 1$ ($y/D = -1$ on the cavity bottom) larger vertical fluctuations are observed in the experiment. The shape of the profile in the incoming flow ($x/D = -0.1$) is very well reproduced but the levels are slightly lower suggesting the mean turbulence level in the incoming flow was slightly lower in the simulation compared to the experiment, which is indeed the case. This may also explain the underestimation of $\overline{v'v'}$ at the two stations. Unlike the variation of $\overline{u'u'}$ in the upstream part of the separated shear layer, the growth of $\overline{v'v'}$ is milder as the stress remains relatively low over the first third of the cavity length. The simulation also predicts quite accurately the vertical fluctuation levels inside the main recirculation eddy (e.g. see sections $x/D = 1.4$ and 1.7 for $y/D < 0$). In the LC, the vertical fluctuations are sharply amplified for $x/D > 1.2$. The quasi-regular shedding of the coherent spanwise vortices induces very high values of the vertical fluctuations close to the trailing-edge. Similarly to the evolution of the vertical stress, the spanwise stress $\overline{w'w'}$ (no measurements are available) starts being amplified substantially inside the shear layer at $x/D = 0.9$ in the TC.

In both simulations the location of the maximum shear stress $\overline{u'v'}$ rises slightly over the mouth of the cavity in the latter half of the cavity. For example, in the TC the maximum shear stress at $x/D = 0.6$ is located almost at the cavity mouth while near the trailing-edge the maximum stress is located at about $0.05D$ above the cavity mouth. This phenomenon was also observed by Neary & Stephanoff (1987). Most probably this is a consequence of the interaction between the large-scale vortices and the trailing-edge. Another possible explanation is that in the turbulent case the turbulent eddies that are convected from upstream of the cavity interact with the eddies inside the shear layer over the cavity. Sometimes the result of this interaction is the formation of a larger coherent structure whose mean position is skewed toward the channel side. The shear stress levels inside the shear layer (figure 5d), especially for $x/D > 1.4$, are accurately predicted by the turbulent inflow simulation. The decay of $\overline{u'v'}$ on the channel side at $x/D = 1.0$ is milder in the simulation; however the same decay is very close to the experimental data at the upstream and downstream stations situated at $x/D = 0.6$ and 1.4, respectively. In the LC, up to $x/D = 1$ the shear stress is almost negligible; however it then grows at a higher rate than in the TC such that the values are comparable near the trailing-edge corner.

4.2. *Instantaneous data and spectral analysis*

The time history of the vertical velocity at three stations situated just upstream of the leading-edge corner (station 6), just downstream of it (7) and just upstream of the
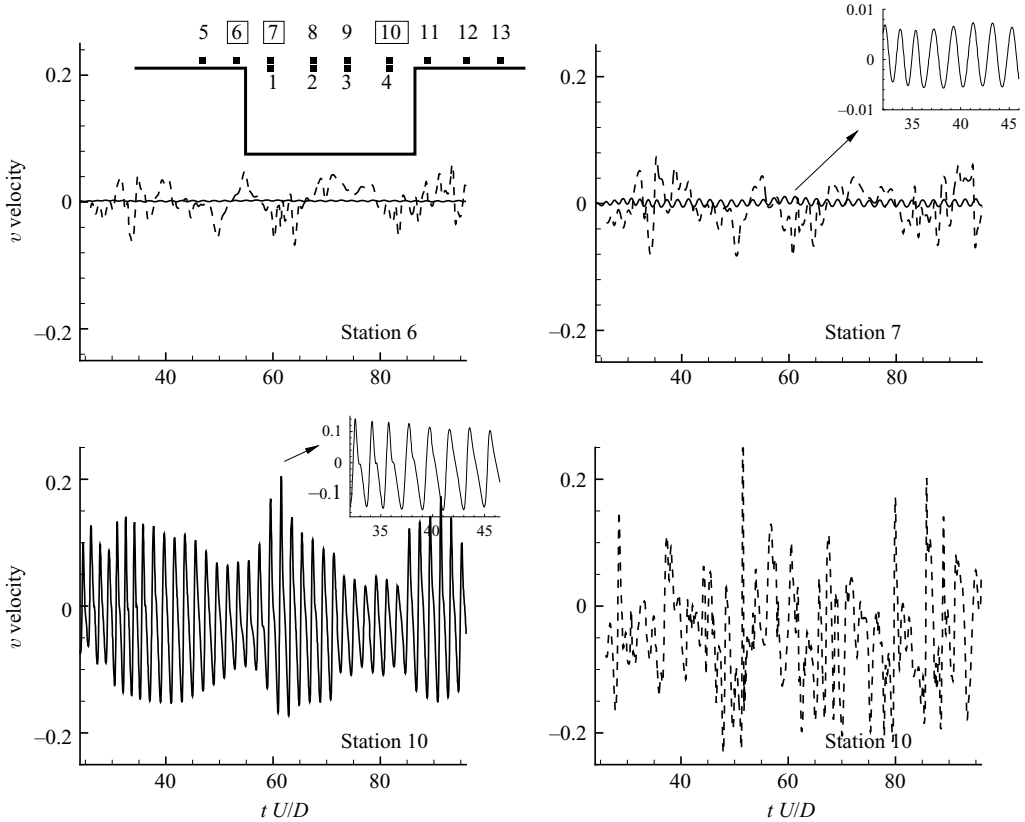
FIGURE 6. Vertical velocity time history for laminar (continuous line) and turbulent (dashed line) inflow cases.

trailing-edge corner (10) are shown in figure 6. In the LC the flow is steady at station 6 (figure 6). Immediately downstream of the separation (station 7), the shear layer starts oscillating regularly (see also inset in figure 6, station 7) at the fundamental frequency corresponding to a Strouhal number $St = fD/U = 0.51$ (figure 7a). The amplitude of these oscillations is growing in the streamwise direction. Concomitantly, very low-frequency modulations are clearly observed in the same time series. We suspect that these very low-frequency oscillations are a consequence of the shear layer interactions with the trailing-edge and with the recirculating motions inside the cavity. The energy associated with these low-frequency oscillations is sensibly smaller than that corresponding to the fundamental frequency. In the LC, the amplitude of the pressure (not shown) and vertical velocity oscillations at the fundamental frequency is amplified by 13–25 times between stations 7 and 10 situated $0.3D$ downstream of the leading edge and $0.4D$ upstream of the trailing-edge. The amplification factor is much smaller (close to two times) in the TC.

Vertical velocity power spectra at stations situated just below (stations 1 to 4) and just over (stations 7 to 10) the cavity mouth ($y/D = 0$) are shown in figure 7 for both cases. Additionally, spectra at two stations (5 and 6) upstream of the cavity leading-edge corner and at three stations (11 to 13) downstream of the trailing-edge corner are included. In the LC, the velocity spectra contain only a few discrete energetic frequencies ($St = 0.51, 1.02, 1.53$ and $St = 0.6, 1.2$) in the region around the cavity. This
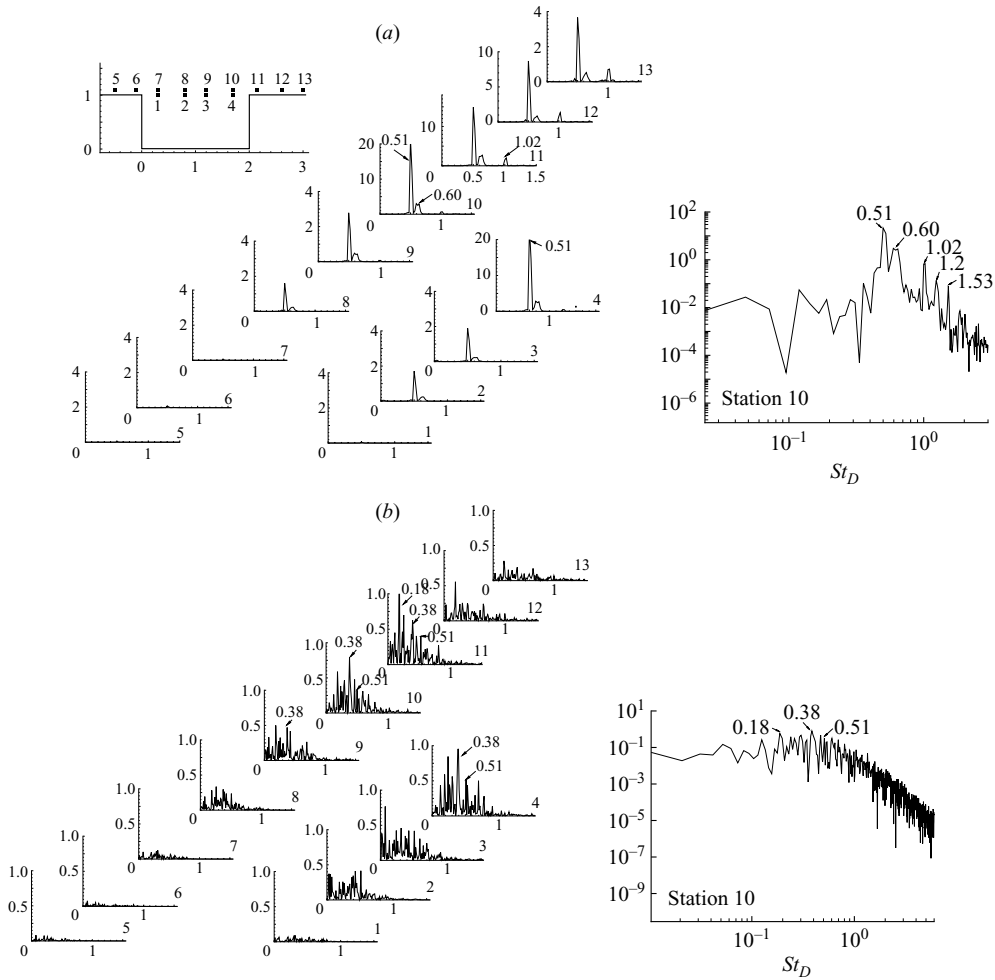
FIGURE 7. Power spectra of vertical velocity for laminar (a) and turbulent (b) inflow cases. The position of the stations is shown in the inset sketch. Spectrum at station 10 is also shown on a log-log scale.

indicates that the flow remains laminar. The growth of Kelvin–Helmholtz instabilities into large-scale oscillations takes place somewhere in between stations 7 ($x/D = 0.25$) and 8 ($x/D = 0.75$). The energy distribution in the spectra at the downstream stations remains qualitatively similar. The most energetic frequency ($St = 0.51$) at all these stations corresponds to the second mode frequency predicted by Rockwell (1977) ($St \sim 0.5$, see figure 7 in his paper with $St_L = 2St$ for $L/D = 2$) for incompressible flow over a cavity with $L/D = 2.0$. The same frequency non-dimensionalized with the momentum thickness of the boundary layer at separation is $St_\theta = f\theta/U = 0.015$. The experimental data of Ethembababoglu (1973) for a cavity with $L/D = 2.0$ and a laminar incoming boundary layer indicate values between 0.49 and 0.58 for the Strouhal number associated with the second mode. For the second mode Sarohia (1977) measured in his experiments over an axisymmetric cavity a Strouhal number in the range $0.41 < St < 0.49$ while Ahuja & Mendoza (1995) found $St \sim 0.55$. In the theoretical model of Howe (1997) the Strouhal number of the second mode for very low-Mach-number cavity flows was predicted to be $St = 0.68$. Alvarez, Kerschen &

Tumin (2004) found $St \sim 0.5$ for the second mode of a two-dimensional cavity flow at $Ma = 0.3$ using their theoretical model. A secondary, much less energetic, frequency is visible in the spectrum at around $St = 0.60$ (along with its first harmonic in the log-log plot of the spectrum) probably due to the three-dimensional jittering effect by the recirculating flow. At the downstream stations the energy of the oscillations associated with the fundamental frequency increases, e.g., by about one order of magnitude between stations 8 and 10 ($x/D = 1.25$). The energy levels associated with the discrete frequencies in the spectra reach their peak at stations 10 and 4 just upstream of the trailing-edge corner and then start decaying downstream of the cavity. The first harmonic of the fundamental mode ($St = 1.02$) is also observed in the spectra downstream of station 9 ($x/D = 1.25$). The log-log spectrum at station 10 shows that even the second harmonic ($St = 1.53$) is relatively energetic. The energy associated with the fundamental frequency decreases sensibly faster than that associated with its first harmonic downstream of the cavity, indicating an increase in the intensity of the nonlinear interactions between the coherent structures (array of hairpin-like vortices) as they are convected past the trailing-edge corner.

In the TC, as the flow upstream of the cavity is fully turbulent, the velocity at stations 5 and 6 displays a broad spectrum with energetic frequencies up to $St < 1.0$. At stations situated downstream of the leading edge corner the energy is increasing considerably (by about eight times between stations 7 and 10) over the whole range of energetic frequencies. Moreover, the energetic part of the spectrum appears to broaden toward higher frequencies ($St < 1.7$). All this indicates an increase in the turbulence intensity and the presence of smaller fairly energetic scales in the separated shear layer as it approaches the trailing-edge. However, the energy amplification within the separated shear layer is not the same for the main energetic frequencies. Up to the trailing-edge the peak in the turbulent spectrum is observed to occur at $St = 0.38$ which corresponds to the first mode predicted by Rockwell's (1977) analysis for flow past a cavity with $L/D = 2$. This frequency is consistent with the estimated value of the mean convection velocity of the coherent structures over the cavity (see discussion of figure 12). It is also interesting to note that Lin & Rockwell (2001) in their experiments with turbulent inflow identified the frequency associated with the formation of large-scale patches of vorticity over the cavity to be $St_\theta = 0.017$ which matches the value predicted by linear stability theory for a convective-type instability. In their experiments this translates into $St = 0.35$ as $D/\theta = 20.32$. This value is close to our predicted value of $St = 0.38$. Ahuja & Mendoza (1995) found $St = 0.35$ and the theory of Howe (1997) for cavity tones in the limit $Ma = 0$ predicts $St = 0.39$ for the first mode frequency. However, these oscillations in the TC are very different to the ones observed in the LC where they were associated with the quasi-regular shedding of two-dimensional spanwise vortices. Due to the large thickness of the incoming boundary layer, no shedding of quasi-two-dimensional structures is observed in the turbulent case. The second mode at $St = 0.51$, though constantly present in the spectra, appears to be less energetic. Starting with station 9, the velocity spectra contain a second very energetic frequency at $St = 0.185$ which is close to the first subharmonic of the fundamental frequency. The presence of this component near the trailing-edge was also observed in the experiments of Lin & Rockwell (2001) in which the incoming flow was turbulent. At downstream stations 12 and 13 the energy is decaying over practically the whole spectrum. Pereira & Sousa (1995) predicted the most energetic frequency to be $St = 0.51$ in their two-dimensional DNS simulations on fairly coarse meshes. In fact, we also predicted a very similar spectrum to that of Pereira & Sousa using three-dimensional detached eddy simulation on grids with about 0.5×10^6 cells
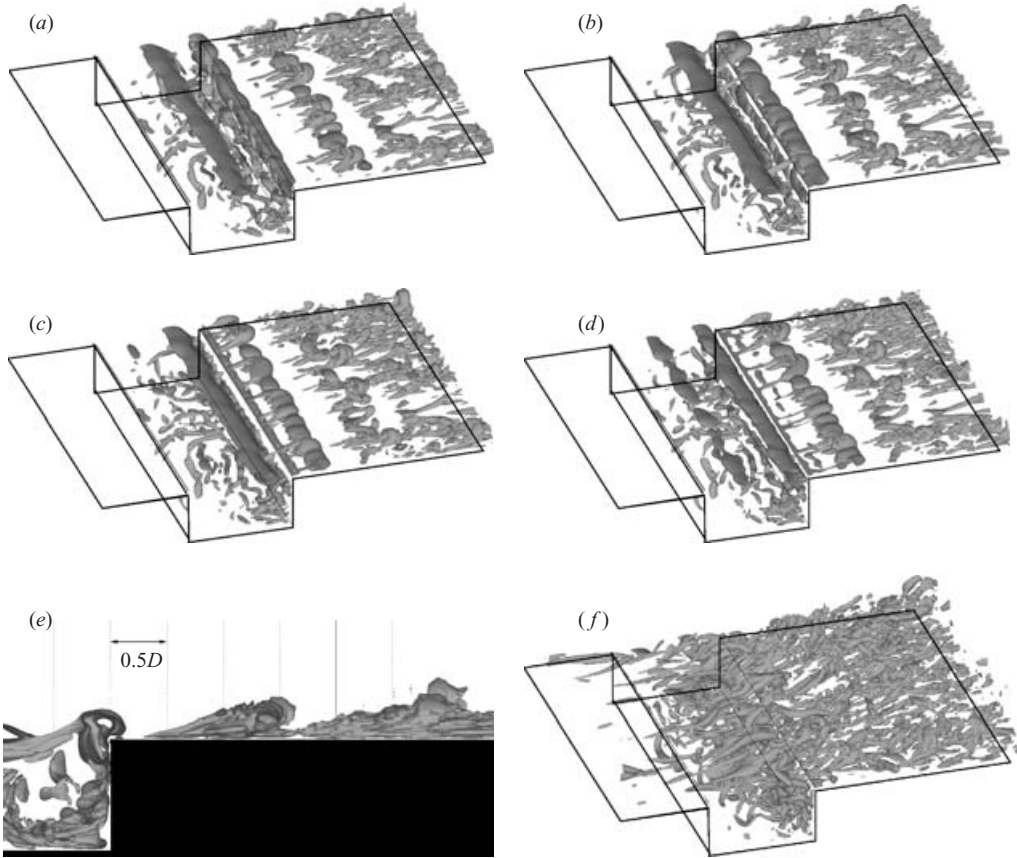
FIGURE 8. Instantaneous coherent structures visualized using the Q criterion in the laminar and turbulent inflow cases; (a) laminar $(T/4)$; (b) laminar $(T/2)$; (c) laminar $(3T/4)$; (d) laminar (T); (e) laminar xy-section $(T/4)$; (f) turbulent.

for the same flow. In these simulations the shedding of the shear layer vortices is quasi-regular and their coherence over the span is very high, which is not the case in the present LES simulation for TC (figure 8f).

4.3. *Coherent structures*

The Q criterion proposed by Hunt, Wray & Moin (1988) was used to educe the vortical structures in figure 8. The isosurface corresponds to $Q = 1.0(U/D)^2$. Figures 8(a) to 8(d) show the coherent structures $T/4$ apart in the LC, where T is the period associated with the fundamental frequency $(St = 0.51)$. Figure 8(e) shows an xy-section through the arrays of hairpin vortices that are convected downstream of the cavity. Figure 8(f) shows the coherent structures in the TC.

In the LC, spanwise aligned vortices are generated in the channel–cavity interface region and eventually interact with the trailing-edge corner. The shedding starts in the downstream half of the cavity and due to the relatively low aspect ratio $(L/D = 2)$ pairing of successively shed spanwise vortices does not occur. A secondary instability acts on these spanwise vortices; it deforms their axis and induces thin streamwise oriented weak vortices which sometimes connect two successive spanwise vortices. The cavity trailing-edge significantly enhances the stretching of the primary spanwise vortices and increases the intensity of three-dimensional vortical structures. The critical

role of the interactions between the spanwise vortices and the trailing-edge corner was also discussed by Rockwell & Knisely (1980). Their observations are consistent with the above discussion. As the spanwise vortex approaches the corner, it is severely deformed. The core is clipped into two parts, one that is convected downward inside the cavity and one that is convected in the streamwise direction very close to the channel bottom downstream of the cavity. As a result of the impingement process, the vorticity convected downstream reorganizes itself into an array of hairpin-like vortices that are generated across the whole span. This array of hairpin vortices (figure 8e) is then convected downstream in a fairly regular fashion. The process is quasi-periodic dictated by the fundamental frequency at which spanwise vortices are shed in the separated shear layer. The mean width of these hairpin-shaped coherent structures is 90 wall units, their length is 240 wall units and their height is around 85 wall units (we used the mean friction velocity in the channel upstream of the cavity to non–dimensionalize the different dimensions). The distance between two arrays of hairpin vortices immediately downstream of the cavity is 180 wall units. As these rows of hairpin structures are convected downstream, secondary instabilities are developing with the effect that some of the hairpins are growing in size while others are diminishing. Sometimes partial merging is observed.

The relatively high level of organization of coherent structures in the LC is practically lost in the TC (figure 8f) due to the jittering of the separated shear layer by the upstream turbulence and by the strong unsteady modulations of the recirculating flow inside the cavity. In fact it appears that the upstream turbulence determines to a great extent the development of disturbances downstream of separation. Snapshots which show the time evolution of the coherent structures educed using the Q criterion do not indicate the presence of any large dominant flow structures. More details about the coherent structures present in the TC can be inferred from vorticity contours in figure 9. Figure 9(a) shows instantaneous out-of-plane vorticity contours in a plane positioned slightly over the cavity mouth at $y/D = 0.05$. Relatively large elongated vorticity streaks formed in the upstream part of the channel (see also the associated streamwise velocity streaks in the same plane shown in figure 16a) are convected over the separated shear layer and are, in most cases, strongly interacting with it. We think that most of these structures are related to the hairpin-like vortices responsible for the formation of the low-speed streaks on the channel bottom. As these streaks of vorticity are convected over the cavity, due to their strong interaction with the separated shear layer and the recirculating flow beneath it, they lose their predominantly elongated shape in the streamwise direction for $x/D > 1$. We shall see (in discussion of figure 16) that the presence of these streaks over the channel can have an important effect in terms of controlling the mass exchange processes between the cavity and the channel. At times, the vorticity and energy levels inside these predominantly streamwise oriented coherent structures are larger than the ones inside the upstream part of the separated shear layer. In the yz-section situated at middle cavity length $x/D = 1$ (figure 9c) one can see how the vorticity sheet is severely disturbed compared to the LC. The vorticity levels around these disturbances are significantly lower. This allows the momentum and mass transfer between the cavity and the flow on top of it to intensify locally. Ejections of fluid from beneath the separated shear layer into the overflow are visible in figure 9(c).

In the xy-section in figure 9(b) (TC) several high-vorticity patches associated with the convection of the near-wall coherent structures from upstream of the cavity are observed. As they move over the cavity these patches of vorticity can be convected over the top or be fully or partially entrained inside it (see also vorticity plots in figure 11).
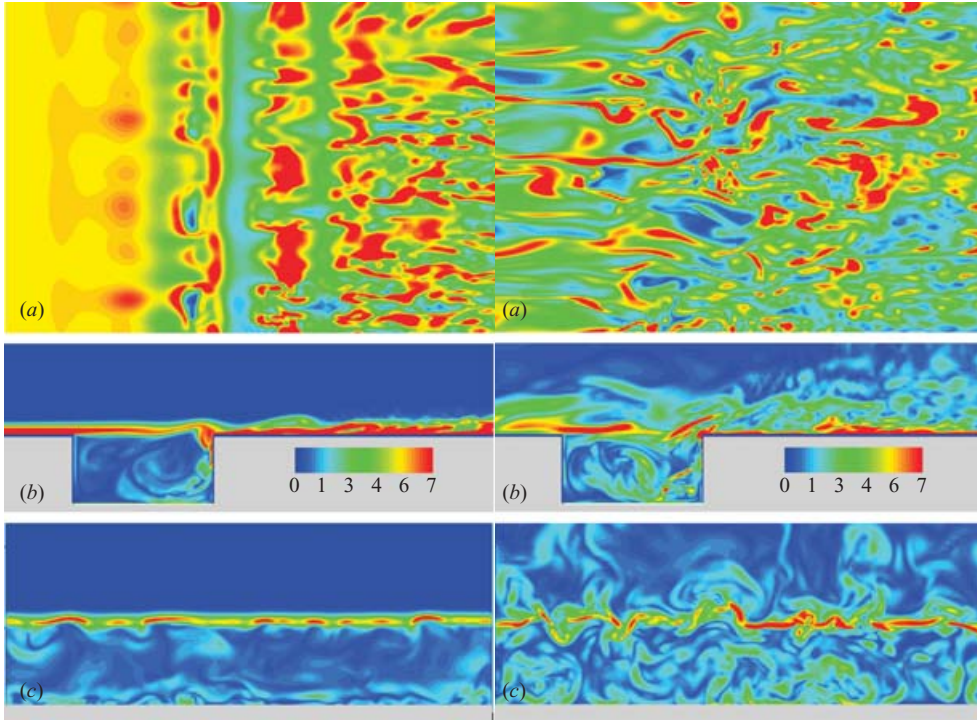
FIGURE 9. Instantaneous vorticity contours for laminar (left) and turbulent (right) inflow conditions. (*a*) out-of-plane vorticity in the $y/D = 0.06$ section; (*b*) vorticity magnitude in an xy-section (*c*) vorticity magnitude in $x/D = 1$ section.

According to Rockwell & Knisely (1980) these events are called complete escape, partial clipping and complete clipping, respectively. The occurrence of one event or another is not deterministic; however, in agreement with the observations of Pereira & Sousa (1994) for the case of a sharp trailing-edge corner, the complete clipping events are found to be less frequent than the other two in the simulation. As the complete escape and partial clipping events are injecting fluid into the jet-like flow parallel to the trailing edge, it is expected that the amplitude of the flow oscillations inside the cavity will increase when such an event happens. Time series of the vertical velocity in the jet-like flow near the trailing-edge and vorticity animations in xy-planes confirmed this phenomenon, also observed in the experiment. As observed in figure 9(*b*), due to the interaction of near-wall eddies coming from upstream of the cavity with the separated shear layer over the cavity, the flow downstream of the cavity appears to be populated with energetic eddies over a larger distance from the channel bottom compared to the flow upstream of the cavity. Moreover, the three-dimensionality of the flow structures in the region downstream of the cavity is clearly higher.

4.4. *Interaction between coherent structures and trailing-edge corner*

Lin & Rockwell (2001) were the first to relate the instantaneous pressure fluctuations near the trailing-edge corner to the instantaneous, global variations of the flow pattern. They found that large-scale pressure variations are produced by the interactions between the large-scale eddies that are convected in the cavity–channel interface region and the trailing-edge corner. This issue is of importance as one can think of geometrical modifications of the shape of the corners that could attenuate
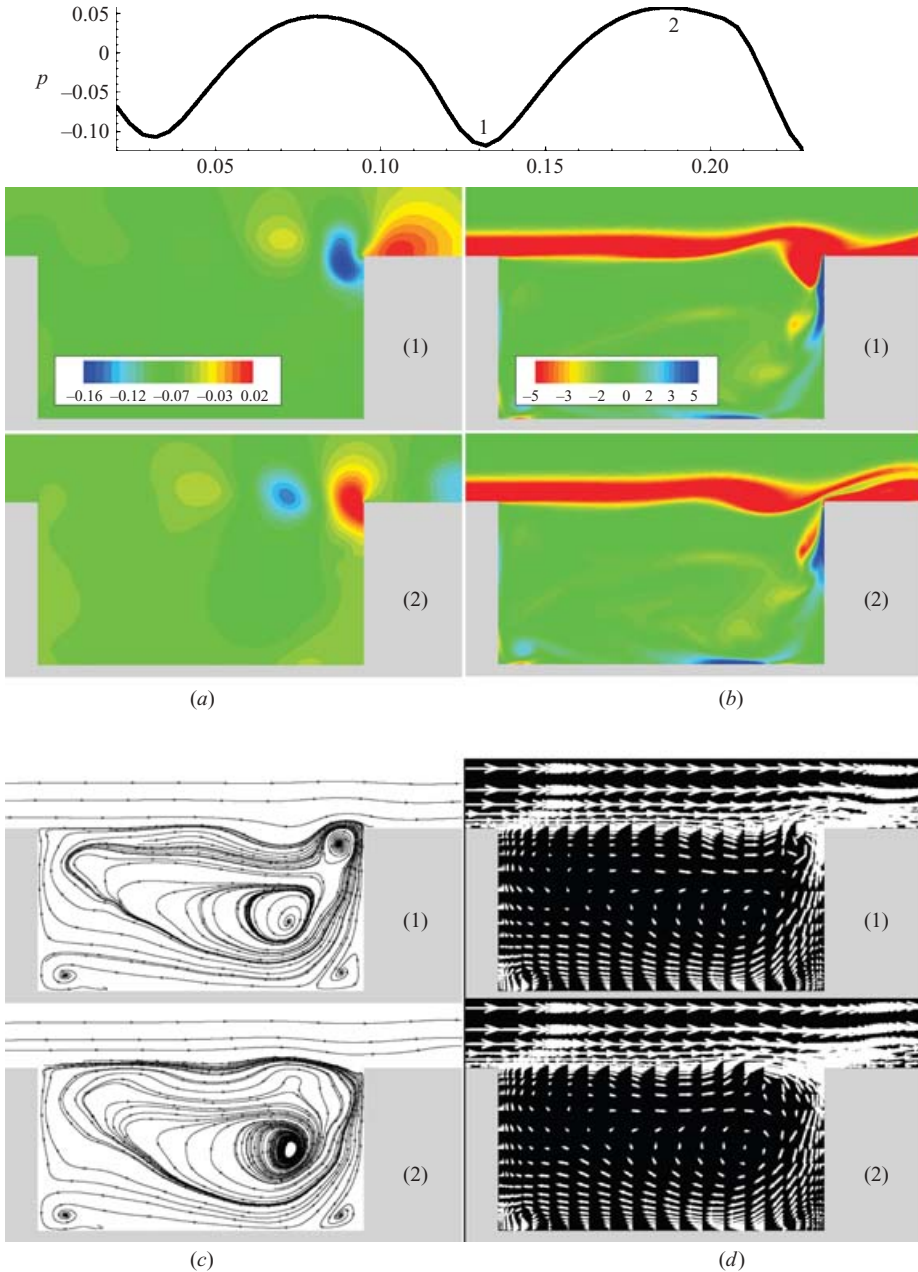
FIGURE 10. Visualizations of flow around the cavity (laminar inflow case) at time instants when a minimum (1) and a maximum (2) value of the pressure at the trailing-edge corner are recorded: (*a*) pressure; (*b*) out-of-plane vorticity; (*c*) two-dimensional streamlines; (*d*) in-plane velocity vectors.

pressure fluctuations inside the critical region near the trailing-edge corner. To clarify this relationship we plot in figures 10 and 11 the pressure time series along with the instantaneous pressure, out-of-plane vorticity, two-dimensional streamlines and velocity vectors (only one in every four grid points are shown in both directions) in
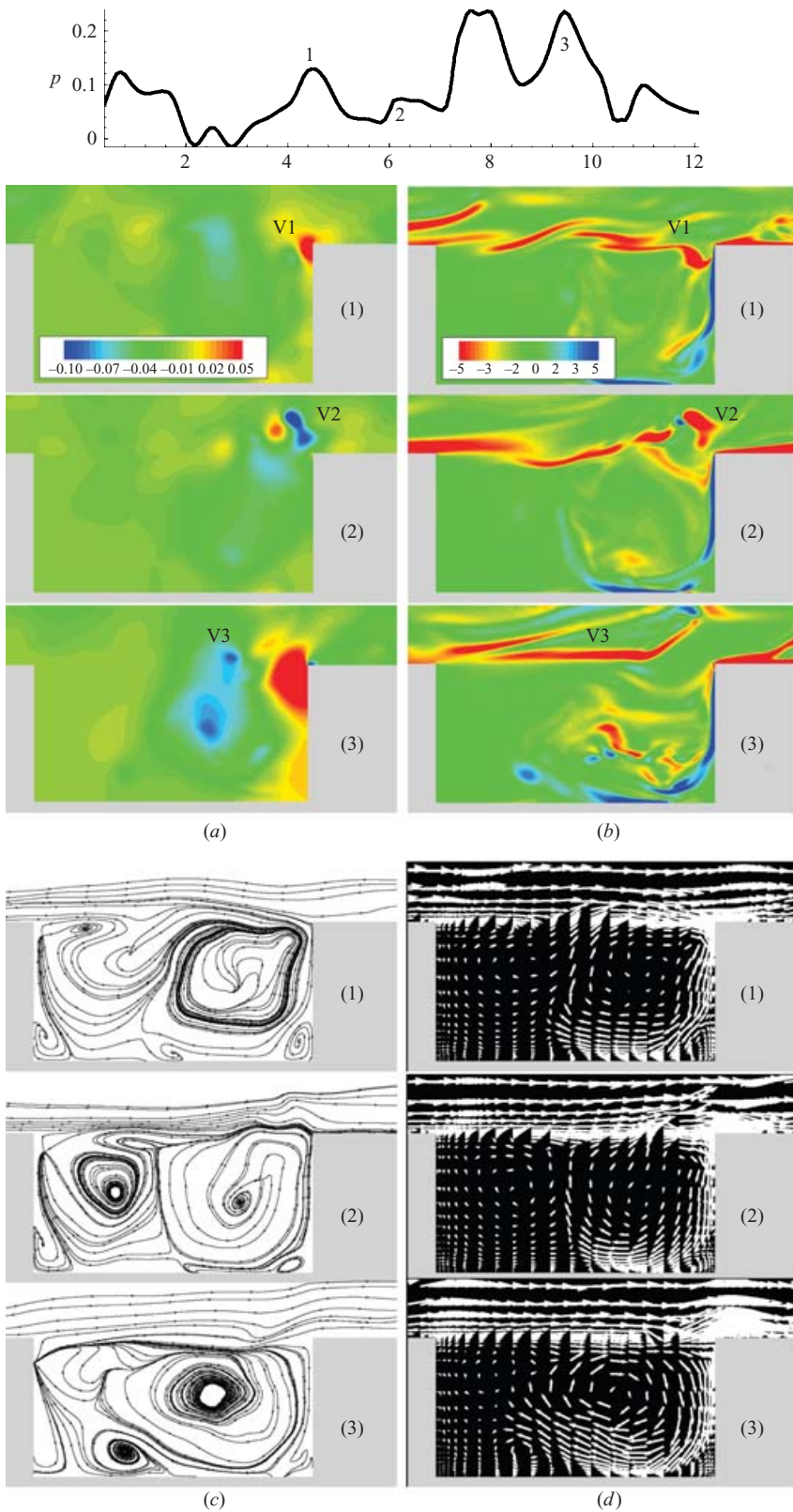
FIGURE 11. For caption see next page.

an xy-section. The instantaneous contour plots are shown at several instants when a pressure minimum or a maximum is recorded near the trailing-edge corner.

In the LC the pressure variation is fairly regular with no substantial modulations between successive peaks. The interaction between the large-scale spanwise vortices and the trailing-edge corner is always in the form of a partial clipping event. As clearly observed in figure 10, the minimum pressure values (e.g. point 1) are recorded during the clipping event when the vortex core, inside which the pressure values are low, starts interacting with the trailing-edge. The approaching vortex is clearly visible in figures 10(a) to 10(c) (frames corresponding to point 1). This event in the shedding cycle corresponds to frame at $t = T/4$ in figure 8(a). The pressure attains its maximum value (e.g. point 2) half of a period later in the shedding cycle ($t = 3T/4$, figure 8c) when the large spanwise vortex is situated at approximately mid-distance between the shedding point and the trailing-edge as observed in figures 10(a) and 10(b). It is also interesting to note the modulations in the intensity of the wall-jet-like flow near the downstream part of the bottom cavity wall where the magnitudes of the velocity vectors are larger in the frame corresponding to a maximum pressure event (point 2). The instantaneous streamlines and velocity vector plots show that the pressure lows are associated with an upward deflection of the flow near the corner while the opposite is observed in the case of a pressure high.

In the TC, the pressure follows a much more complex variation in which the values corresponding to successive highs and lows can be quite different. Examination of pressure time series and of the pressure spectrum show that usually the time interval between two successive minimum or maximum pressure values is close to $T = 2.63D/U$ corresponding to the most energetic frequency in the separated shear layer ($St = 0.38$). However, the time interval is sometimes closer to twice that value which corresponds to its first subharmonic ($St = 0.19$). This is confirmed by the velocity spectra in figure 7 at stations 10 and 11 close to the trailing-edge corner where these two frequencies are the most energetic. The presence of pressure highs and lows spaced mostly at T or $2T$ in time is in agreement with the findings in the experimental study of Lin & Rockwell (2001). Three representative events corresponding to points 1, 2 and 3 in figure 11 were selected for further analysis. Point 1 corresponds to a relative pressure maximum but the value of the pressure is lower than that recorded at point 3 which is representative of the largest pressure peaks observed to occur over a large time interval. Point 2 corresponds to a pressure minimum. The pressure and vorticity contours corresponding to point 1 show that around this time a complete clipping event takes place. The patch of vorticity denoted V1 is clearly going to be fully entrained into the cavity. As V1 is at a level below the cavity mouth, the pressure at the trailing-edge remains relatively high. Still, the interaction with V1, inside which the pressure values are lower, reduces the normal peak values recorded for time instants when no patch of vorticity was present near the trailing-edge corner (e.g. point 3). In the case of point 2, a complete escape event is observed in which a patch (V2) of high vorticity and very low pressure values is convected over the trailing-edge corner. As V2 is swept just above it, the pressure at the trailing-edge corner is reduced and fluid is ejected out of the cavity (see corresponding velocity vector plot in the region

FIGURE 11. Visualizations of flow around cavity (turbulent inflow case) at time instants when a relative maximum (1), a minimum (2) and a maximum (3) value of the pressure at the trailing-edge corner are recorded: (a) pressure; (b) out-of-plane vorticity; (c) streamlines; (d) in-plane velocity vectors.
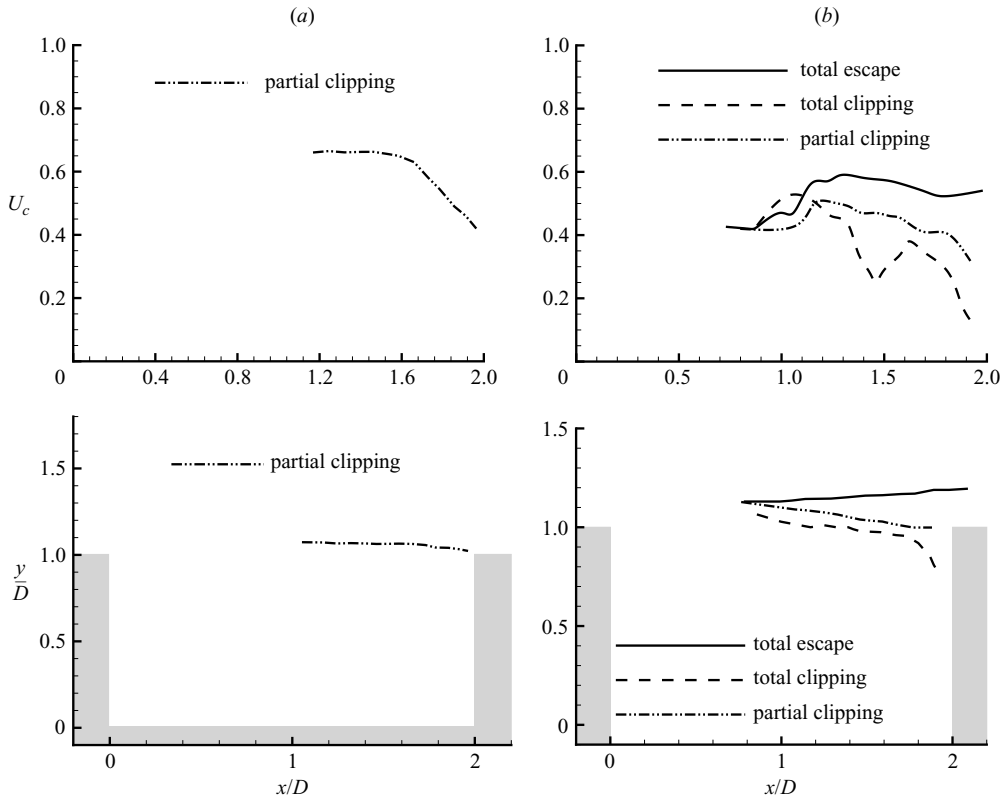
FIGURE 12. Convective velocity (top) and trajectories (bottom) of the structures convected on top of the cavity in the laminar (*a*) and turbulent (*b*) inflow cases.

around the cavity mouth at $x/D \sim 1.5$). Observe also that in this case the streamlines just over the trailing-edge corner are deflected upwards in contrast to the downward deflections observed in the same region at the time instances corresponding to points 1 and 3. Finally, point 3 corresponds to a high pressure peak. In this case the vorticity plot shows no patches of vorticity in the vicinity of the trailing-edge corner. A streak of high vorticity denoted V3 has just passed the middle of the cavity but is still far from the corner. Regarding the modulations in the intensity of the jet-like flow, comparison of the snapshots corresponding to the three events suggests that when the pressure near the trailing-edge corner is at a minimum the width of the jet-like flow near the cavity bottom is smaller and the velocity magnitude inside it is higher.

Figure 12 shows the mean trajectories and convection velocities of the coherent structures starting at the position where spanwise vortices are shed (close to mid-cavity length in LC) or where patches of vorticity are clearly distinguishable (TC). The convective velocity was determined from analysis of successive frames showing the evolution in time of vortical structures near the cavity mouth in xy-planes.

In the LC the spanwise vortices are convected for $1 < x/D < 1.6$ with a (phase-averaged) convective velocity roughly equal to $U_c(x)/U \sim 0.65$. Then, as they start interacting with the trailing-edge corner, they decrease their velocity to about $0.4U$. The convective velocity over the plateau region ($1 < x/D < 1.6$) is very close to the values observed in the simulation of Larcheveque *et al.* (2003) and in the experiments by Ahuja & Mendoza (1995) for large structures in a weakly compressible resonant

cavity. The mean convection velocity inferred from figure 12 in the LC is $U_{cm}/U \sim 0.55$. The mean convection velocity over the region where shedding is present appears to be close to the value inferred from Sarohia's (1977) results for the propagation speed of the second modes of cavity oscillations ($L/\delta = 11.1$ in LC) which is equal to $0.52U$. One should also observe that applying Rossiter's (1964) formula in the limit of $Ma = 0$ with a value of the phase delay of 0.25 and the above-determined mean convective velocity, one obtains for the second mode a value of the Strouhal number $St \sim 0.48$ which is close to that measured in the velocity spectra in figure 7.

In the TC the trajectories are analysed as a function of the type of interaction of the coherent structure with the trailing-edge corner. As the formation of these structures is random, the plots in figure 12 for the TC correspond to averages over ten realizations for each kind of interaction. For the eddies that will be finally entrained into the cavity (total clipping) the mean convection velocity is the smallest and shows the largest variations with the streamwise position. This is expected because of the complex interactions with the eddies inside the cavity. We suspect that the relative maximum at around $x/D = 1.7$ is due to the interactions with the patches of vorticity convected at a larger velocity that are associated with a partial clipping event. Observe that at that location the trajectories associated with the two kinds of events are very close to each other. The eddies that will be convected over the cavity (total escape events) appear to attain a practically constant velocity for $x/D > 1.2$ equal to $0.55U$. Probably this is due to the fact that once they are convected slightly over the cavity channel interface, they interact very little with the other energetic eddies that populate the shear layer region. From the plots in figure 12 for the TC one can infer a mean 'global' convection velocity regardless of the type of interaction between the eddy and the trailing-edge corner. Its value is $U_{cm}/U \sim 0.41$.

4.5. *Mass exchange processes between cavity and channel*

The instantaneous scalar concentration plots in an xy-plane in figure 13 suggest that in the LC most of the mass exchange between cavity and channel is taking place over the downstream part of the separated shear layer where large spanwise vortices are shed. Figure 14 helps to elucidate the role played by these vortives in the scalar ejection process. The instantaneous pressure contours at the cavity–channel interface ($y/D = 0$) are shown in figure 14(a). The core of the vortex corresponds to the narrow band of low pressure levels. The axis of the vortex is marked with the dashed line. Its position is also indicated in figure 14(b) showing the vertical velocity and in figure 14(c) in which the scalar concentration contours are plotted at the same time instant. As observed in figures 14(b) and 14(c), the spanwise vortex is convecting low-concentration fluid from the channel toward the cavity on its upstream side (relative to its axis) and high-concentration fluid from inside the cavity toward the channel on its downstream side. This is evident as the region of high-concentration fluid is practically the same as the band where the vertical velocity is positive (outflow region), while the region downstream of the vortex axis contains low-concentration fluid and the vertical velocity is negative (inflow region). The mass transport process is fairly uniform in the spanwise direction, though some variations due to the three-dimensional perturbations of the core of these vortices can be observed over the span. Though figure 14 illustrates the effect of the spanwise vortices on the scalar transport at an isolated moment in time, the process is very similar over the whole shedding cycle. Most of the high-concentration fluid entrained by the spanwise vortices is then convected downstream of the trailing-edge corner. The streaks of relatively high-concentration fluid observed on the channel bottom downstream of the cavity
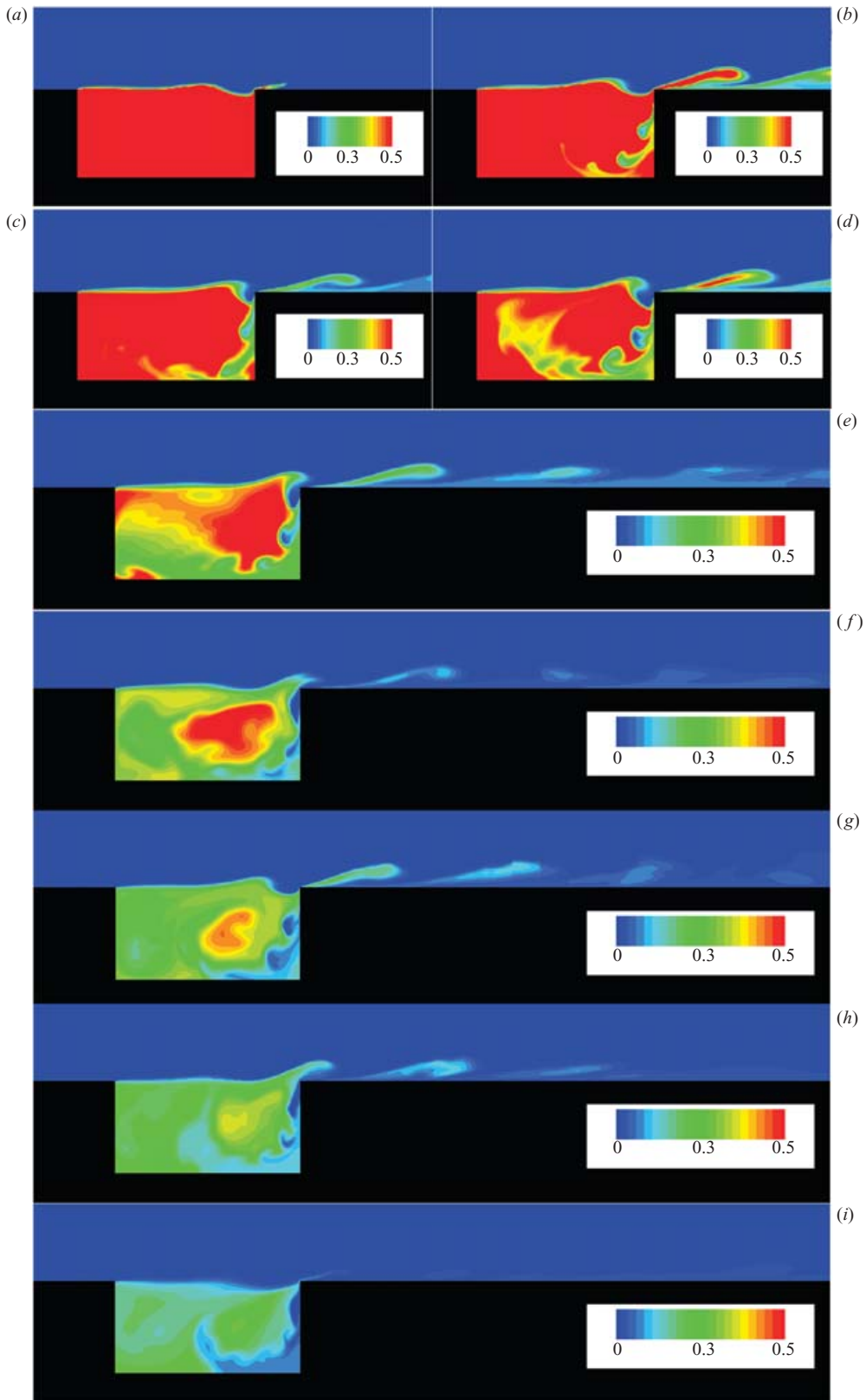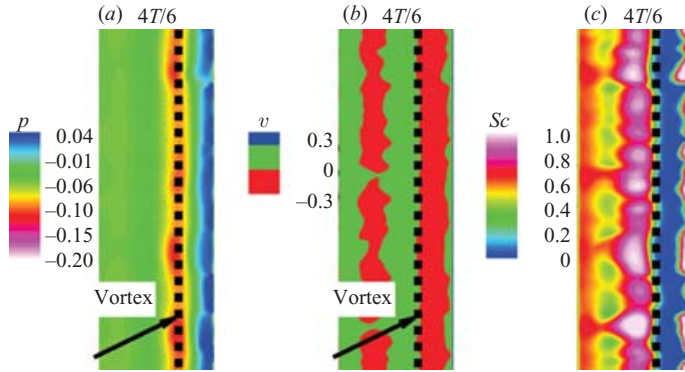
FIGURE 13. For caption see next page.

FIGURE 14. Instantaneous distributions of pressure, vertical velocity and scalar in the $y/D=0$ section in the laminar inflow case.

(e.g. see figures 13*e* and 13*g*) correspond to the arrays of hairpin-like vortices in figure 8.

The patches of low-concentration fluid injected into the cavity are entrained into the jet-like flow in between the core of the recirculation region and the cavity walls (e.g. see figure 13*d*). As these patches are convected inside the jet, they mix with the high-concentration fluid around them. This illustrates the critical role of the jet-like flow in intensifying the mixing inside the cavity. In the LC the main recirculation region extends over most of the cavity (see figures 2*a* and 10*c*) and thus the mixing in the upstream part of the cavity is relatively high. For $t > 80D/U$ (frames *e* to *i* in figure 13) the highest concentrations are observed inside the central region of the main recirculation eddy. Eventually this high-concentration fluid diffuses away from the central region and is mixed with the surrounding lower concentration fluid.

In the TC, initially (figure 15*a*) most of the scalar exchange between channel and cavity is due to the engulfing of high-concentration fluid from the cavity by the eddies that populate the interface region. During partial or complete clipping events patches of low-concentration and relatively high-vorticity fluid are pushed downward parallel to the trailing-edge of the cavity and then recirculated by the jet-like flow (similar to the LC) inside the downstream half of the cavity. The mixing of these low-concentration eddies with the surrounding high-concentration fluid inside the centre of the main recirculation eddy and with the fluid situated in the upstream part of the cavity occurs at a higher rate than in the LC because of the presence of small-scale three-dimensional eddies throughout the cavity (see also figure 9*c*). This process is clearly visible in figures 15(*c*) and 15(*d*). The correlation between the jet-like flow and the advection of the low-concentration patches of fluid inside the cavity is evident by comparing figure 15(*c*) with the velocity vector plots in figure 11(*d*). At times, due to modulations in the jet intensity and direction, once it separates from the bottom cavity, the main recirculation eddy is increasing in size and squeezes the high-concentration fluid in the upstream recirculation eddy. This has the effect of pushing the top right corner of the upstream recirculation eddy into the separated
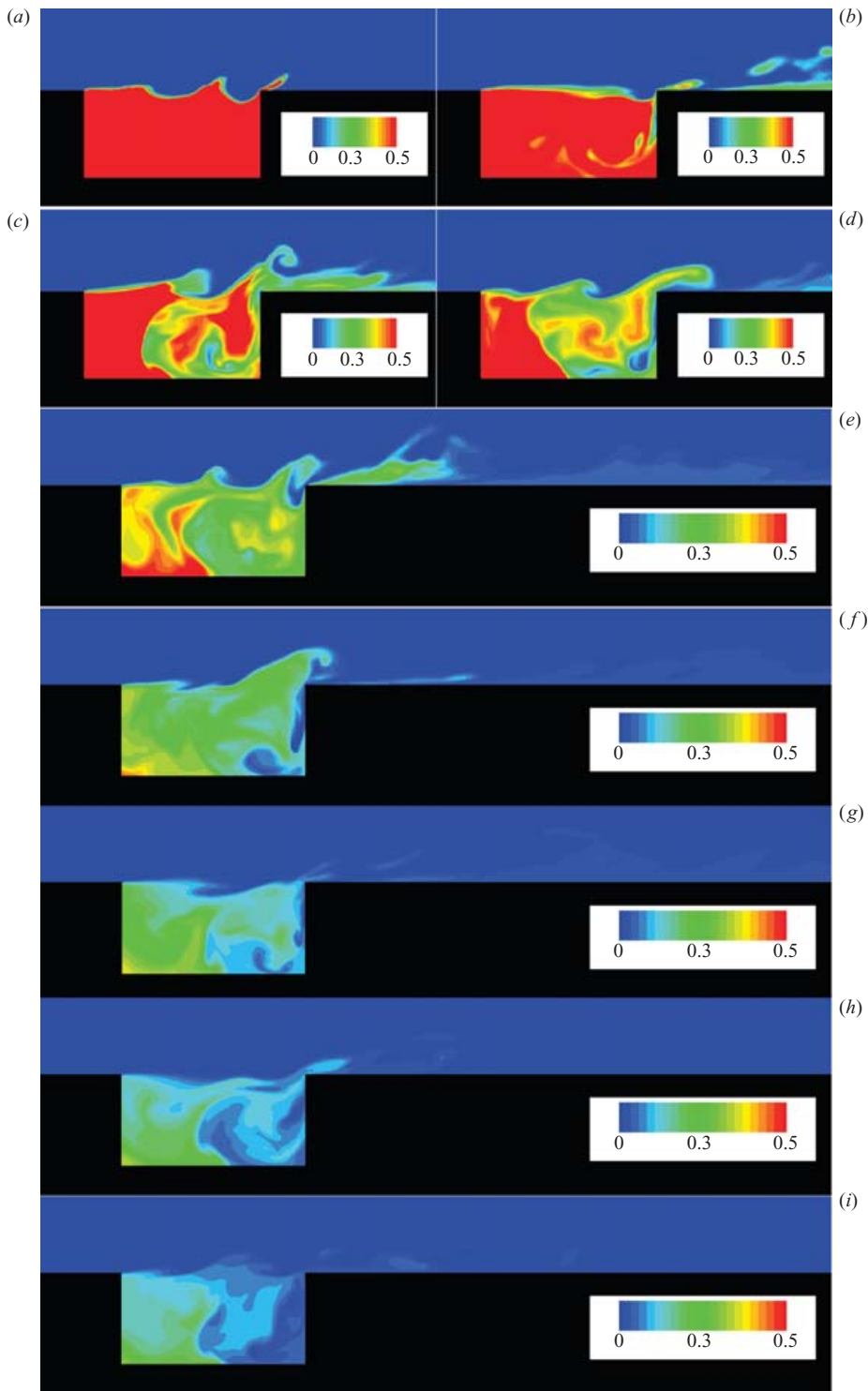
FIGURE 13. Instantaneous contours showing evolution of scalar concentration in an xy-section for laminar inflow case. (*a*) $tU/D=2.0$, (*b*) 20, (*c*) 40, (*d*) 60, (*e*) 80, (*f*) 100, (*g*) 120, (*h*) 140, (*i*) 160.

FIGURE 15. Instantaneous contours showing evolution of scalar concentration in an xy-section for turbulent inflow case. (*a*) $t\,U/D = 2.0$, (*b*) 20, (*c*) 40, (*d*) 60, (*e*) 80, (*f*) 100, (*g*) 120, (*h*) 140, (*i*) 160.

shear layer and also inducing further disturbances into the shear layer. Animations of the mass exchange process show that at these moments some high-concentration fluid from the top part of the secondary recirculation eddy escapes the cavity. However, only a small amount of high-concentration scalar trapped originally in the upstream (secondary) recirculation eddy is able to leave the cavity through the upper part. This is because the separated shear layer even in the TC is at most times just a vorticity sheet extending over the first third of the cavity that does not allow any large-scale mixing via engulfing. Another entrainment mechanism present only in the TC is due to the action of the streamwise oriented coherent structures originating from the near-wall region of the channel bottom (figure 16a) which in some cases can extract fluid from beneath the separated shear layer including from its upstream part.

Figures 16 and 17 help to clarify the role played by the near-wall quasi-streamwise vortices present on top of the cavity in the mass exchange process. Djenidi, Elavarasan & Antonia (1999) in an experimental study of the flow over an array of two-dimensional square ($L/D = 1$, $L/\theta \sim 3$) cavities placed transversely to the flow direction observed that the occurrence of inflows and outflows from and into the cavity was random. They also observed that these events were associated with the passage of quasi-streamwise vortices and the corresponding low-speed streaks over the array of two-dimensional cavities. Their visualizations showed that low-speed streaks were present in the layer on top of the cavities, similarly to the case of the flow over a smooth wall. In our case the cavity ratio L/D is twice the one in the experiment of Djenidi *et al.* (1999) while $L/\theta = 7.3$, and it appears that on average the low-speed streaks maintain their orientation and coherence only over the first half of the cavity length (up to $x/D \sim 1$). This can be observed from the streamwise velocity contours in a plane situated at $y/D = 0.06$ in figure 16(a). Occasionally some of the streaks extend over the whole cavity length and some distance downstream of it. However, on average, due to the interaction with the eddies inside the separated shear layer that is additionally disturbed by the recirculation flow inside the cavity (especially for $x/D > 1$), the streaks lose their predominantly streamwise orientation and increase their width and three-dimensionality over the downstream half of the cavity and past it. The interaction between the streaks and the separated shear layer is very clear in animations. It is also apparent in the vorticity contours in figure 11(b). In fact, over the downstream half of the cavity it is very hard to distinguish between the vortical structures that originated from the separated shear layer and the ones associated with the streaks on top of it.

As the flow is incompressible, at each moment of time the sum of the outflows over the cavity mouth ($y/D = 0$) should be balanced by the sum of the inflows. In the case of the mass exchange process, the inflows are generally associated with convection of low-concentration fluid inside the cavity, and the outflows with ejection of higher concentration fluid from the cavity. Animations of the flow on top of the cavity over large periods of time has shown that the occurrence of the inflows and outflows is random, and in many cases the inflow or outflow regions are persistent for relatively long intervals of times (of the order of $1 - 10D/U$). In fact, the events when outflow/inflow regions maintain their character for long time intervals appear to be predominantly the ones that are due to the presence of streamwise streaks over them. Such an event is visualized in figure 17 where the streamwise velocity, concentration and vertical velocity contours are plotted at the cavity–channel interface. Four frames at an interval of $1.3D/U$ apart are shown.

A first interesting observation is that consistently the outflow regions correlate with the ones in which the streamwise velocity is relatively low (the high-momentum
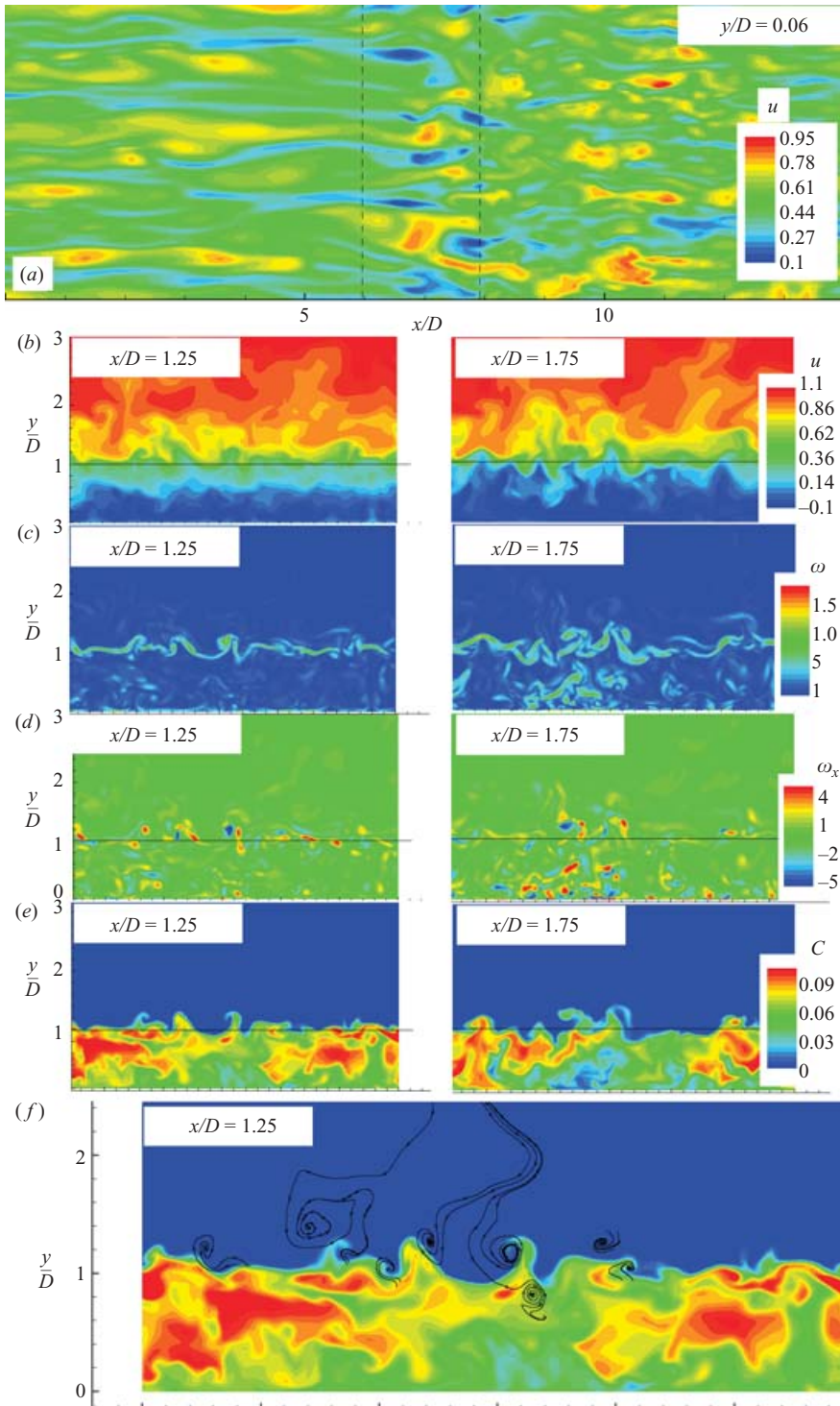
FIGURE 16. Visualizations of the instantaneous flow structure and scalar transport around the cavity. (*a*) streamwise velocity, $y/D = 0.06$; (*b*) streamwise velocity, $x/D = 1.25$ and 1.75; (*c*) vorticity magnitude, $x/D = 1.25$ and 1.75; (*d*) streamwise vorticity, $x/D = 1.25$ and 1.75; (*e*) scalar concentration, $x/D = 1.25$ and 1.75; (*f*) detail showing the streamwise vortical structures near the interface visualized using two-dimensional streamlines, $x/D = 1.25$.
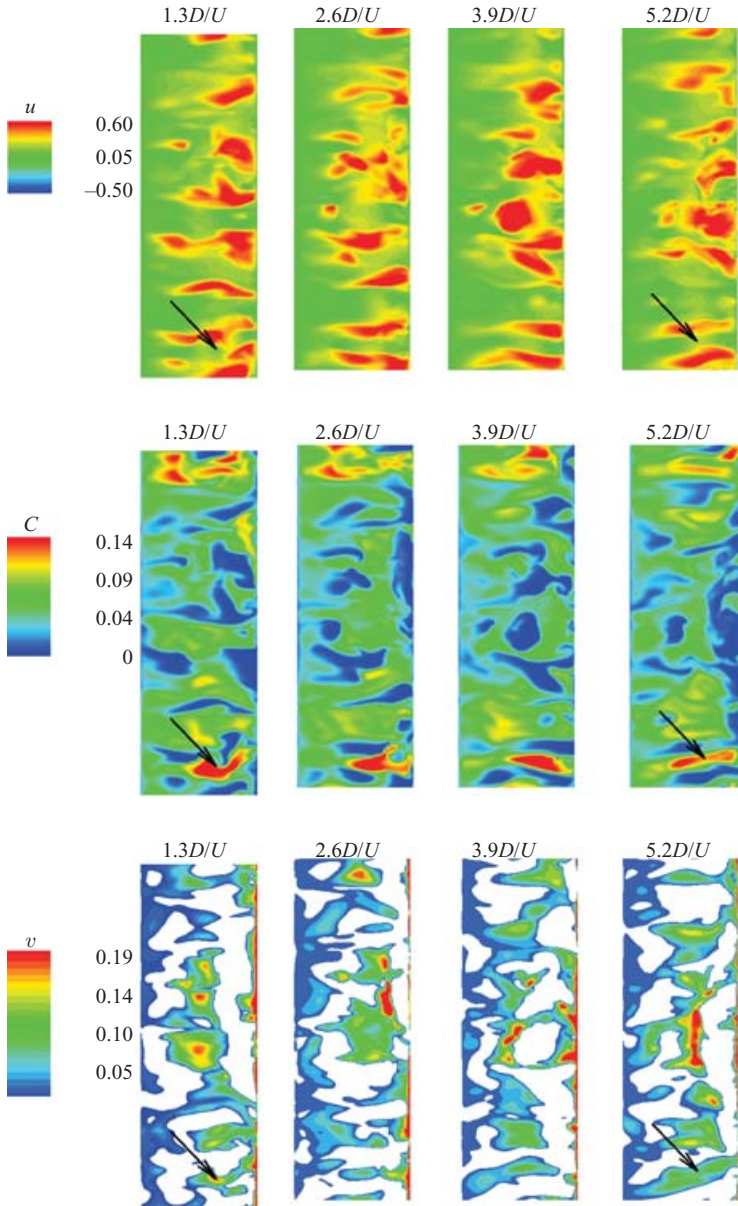
FIGURE 17. Instantaneous distributions of streamwise velocity, scalar concentration and vertical velocity (negative regions are blanked) at the cavity–channel interface ($y/D = 0$) in the turbulent inflow case.

regions in the streamwise velocity contour plots correlate with the blanked inflow regions in the vertical velocity contour plots). The regions characterized by a relatively high concentration appear to be a subset of the outflow regions. The low-momentum fluid trapped inside the cavity is more easily entrained into the channel, hence the correlation between the outflow regions and the low-streamwise-velocity regions on top of the cavity. The occurrence of an outflow can further perturb the flow and the originally streamwise oriented streaks and thus increase the three-dimensionality of

the flow over the downstream part of the cavity and the formation of small-scale vortical structures.

A second observation from figure 17 is the presence of two high-velocity streaks that extend over most of the cavity length toward the bottom of these frames. In between them a region of high positive vertical velocities and high concentration is observed in all four frames (the arrow points toward it). Meanwhile, over this time the high-speed streaks maintain their coherence while slowly changing their position and intensity. This strong outflow region formed as a consequence of eddies being advected in the overlaying flow just over the separated shear layer. The counter-rotating streamwise vortices associated with these velocity streaks were able to break the vorticity sheet associated with the separated shear layer and entrain high-concentration fluid from beneath. The ejected high-concentration fluid is then convected downstream. Evidence of this kind of event is offered in figures 16(b) to 16(e) which show the streamwise velocity, total vorticity, streamwise vorticity and concentration in two yz-sections situated at $x/D = 1.25$ and $x/D = 1.75$. The total vorticity is a good indicator of the position of the vorticity sheet on top of the cavity. The deformation of the vorticity sheet and the probability the sheet will break up, allowing the relatively high concentration fluid from below to escape, are increasing as the trailing-edge is approached. This can be observed by comparing the two frames in figures 16(c) and 16(e). Mushroom-like eddies are observed in regions where patches of vorticity associated with the presence of relatively strong counter-rotating streamwise vortices are present near the cavity–channel interface. The axis defined by these vortices is not necessarily parallel to the interface which explains why the direction of the high-concentration intrusions is not always perpendicular to the interface. In some cases, depending on the rotation direction of these counter-rotating vortices, low-concentration fluid can be injected into the cavity. These events are clearly observed in figures 16(b) to 16(e) in which the locations where high-concentration fluid is entrained into the low-concentration region correlate well with the positions where pairs of patches of streamwise vorticity of opposite sign are present, with the deformation of the vorticity sheet on top of the cavity and with the locations where low streamwise momentum fluid is present over the channel–cavity interface. More evidence of the fact that the intrusions of high-concentration fluid over the mean interface between the low- and high-concentration regions correlate with the presence of patches of streamwise vorticity is given in figure 16(f) in which two-dimensional streamlines were superimposed on the concentration field in the $x/D = 1.25$ section.

Finally, we analyse in a quantitative way the influence of the flow conditions upstream of the cavity on the ejection of the scalar from the cavity. Figure 18 shows the decay in time of the scalar mass inside the cavity plotted in a log-linear scale. The time needed to eject 90 % of the scalar introduced inside the cavity is about $166D/U$ in the TC and $208D/U$ in the LC. Especially in environmental engineering, one-dimensional models relying on empirical dispersion coefficients (Uijttewaal, Lehmann & van Mazijk 2001) are used to globally describe the mass exchange between cavities and the main channel. These models simply assume that the local rate of decay of scalar/pollutant mass inside the cavity is proportional to the mean concentration difference between the channel and cavity. If this law is assumed, then the decay of the scalar mass in time is exponential $M/M_0 = \exp(-t/T_0)$ where T_0 is the characteristic time scale and M_0 is the initial mass of scalar inside cavity. If one non-dimensionalizes T_0 using D and U, one obtains the so-called non-dimensional exchange coefficient k_0. A constant value of k_0 corresponds to a linear variation of the total mass in time,
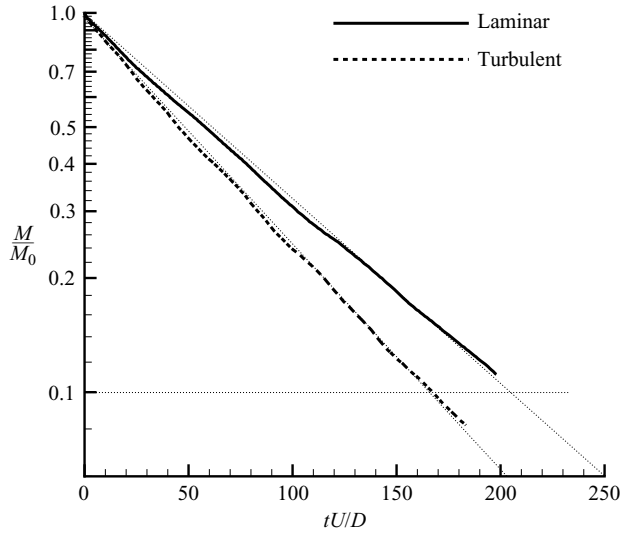
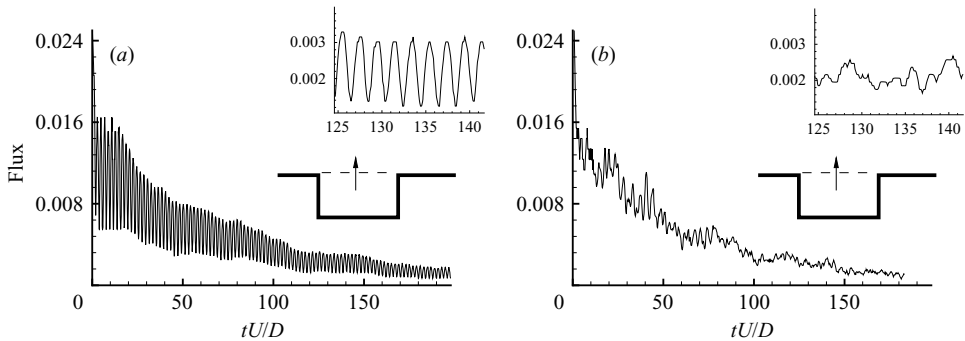FIGURE 18. Variation of scalar mass inside the cavity.

FIGURE 19. Variation of instantaneous flux through the cavity–channel interface for laminar (*a*) and turbulent (*b*) inflow cases.

if the mass is plotted in a log scale. Figure 18 strongly suggests that the decay can be approximated fairly well by a straight line over the whole duration of the decay process (less than 10 % of initial scalar mass left inside cavity) for both simulations. This is in contrast to the ejection of fluid from a channel with a bottom cavity and a lateral sidewall (McCoy, Constantinescu & Weber, 2005) where the ejection process has two phases. In that case, both the initial and final phase can be described using the simple one-dimensional model but the associated values of the exchange coefficient are different. In the present turbulent inflow simulation the inferred value of k_0 is 0.015 which is in the expected range for the given flow conditions and cavity sizes. For the LC, the value is about 15 % lower, $k_0 = 0.013$.

A more detailed understanding of the way the scalar leaves the cavity is given by the time history of the mass flux ($\int Cv \, DA$) through the cavity–channel interface surface which is shown in figure 19. In the LC, at the start of the scalar ejection process the value of the mean flux is the largest. The decay of the mean flux appears to be close to exponential and is modulated by the oscillations due to the engulfment of high-concentration flow from inside the cavity by the spanwise vortices

convected over the second half of the cavity. These oscillations are taking place at the fundamental oscillatory frequency ($St = 0.51$) and can be clearly observed in the inset in the corresponding frame in figure 19. In the TC, the mean decay appears to be qualitatively similar though the high-frequency oscillations do not occur at a discrete frequency at any stage of the ejection process. This is somewhat expected, as the mass exchange process is determined in a great measure by the interaction between the near-wall structures convected from upstream of the channel and the separated shear layer as well as by the nature of the interactions between the patches of vorticity that populate the region around the interface. These interactions are relatively random and thus no clear oscillatory frequency is observed for the scalar flux in the TC.

5. Summary

The three-dimensional incompressible flow past a rectangular two-dimensional cavity in a channel was investigated using LES. Two simulations at the same cavity Reynolds number ($Re_D = 5000$) in which a developing laminar boundary layer (LC) and a fully turbulent flow (TC) were present at the leading cavity edge were performed. As these simulations were carried out in the absence of any acoustic resonant phenomena, the complex phenomena associated with resonant cavities were not present. In both cases it was found that the resolved stresses in the downstream part of the separated shear layer dominate those of the cavity region and approaching boundary layer (turbulent case only) and that the injection of patches of large-scale vorticity inside the cavity near the trailing-edge corner induces important modulations of the jet-like flow that develops near the cavity trailing-edge and bottom. This jet-like flow was found to induce further oscillations of the separated shear layer.

In the LC, the predicted dominant frequency in the shear layer ($St = 0.51$) was found to agree well with the second mode frequency predicted by Rockwell (1977). The velocity spectra at different locations around the cavity showed that the flow remained laminar over the whole domain. The growth of three-dimensional instabilities originating at the leading edge induced deformations of the cores of the spanwise vortices that were shed quasi-regularly in the separated shear layer. The spanwise vortices were found to break into an array of hairpin-like vortices as a result of their interaction with the trailing-edge corner which resulted in a partial clipping event. In the TC, a broad spectrum was observed over the whole length of the separated shear layer. The jittering of the separated shear layer due to the interaction with the incoming turbulent eddies from the near-wall region upstream of the cavity was very strong. As a consequence, the quasi-regular shedding of large spanwise structures observed in the LC was not present. The interaction between the large-scale eddies that populate the region around the cavity mouth and the trailing-edge corner was found to be random.

Observation of the mass exchange process between a scalar introduced instantaneously inside the cavity and the channel showed that injection of patches of low-concentration fluid near the trailing-edge enhanced the scalar mixing inside the cavity in both cases. The simulations also showed there are important differences between the mechanisms responsible for scalar transport and ejection in the two cases. In the LC the main mechanism is very simple and consists of simultaneous engulfment of low-concentration fluid from the channel that is convected into the cavity and of high-concentration fluid from below the cavity–channel interface that is convected into the channel by the large-scale spanwise vortices. This exchange occurs over the downstream half of the interface. In the TC, though engulfment near the

interface is still important, it does not take place more or less uniformly over the span as was the case in the laminar simulation. The separated shear layer is strongly perturbed by interactions with the eddies advected from upstream of the cavity and with the highly three-dimensional eddies inside the cavity that are convected by the jet-like flow toward the shear layer. The engulfment takes place randomly and can be observed over a larger region of the interface compared to the laminar case. An additional mechanism, also induced by the near-wall coherent structures advected from upstream of the cavity, is due to the presence from time to time of strong counter-rotating vortical structures on top of the cavity associated with low-speed streaks similar to the ones observed in the flow over a smooth wall. Sometimes these streamwise oriented coherent structures are strong enough to break the vorticity sheet associated with the separated shear layer and to entrain substantial amounts of high-concentration and low-momentum fluid from beneath. In both cases it was found that the decay of the passive scalar mass inside the cavity can be approximated well by a simple one-dimensional dead-zone model which assumes an exponential decay of the mean concentration inside the cavity in time. Moreover it was found that a single-valued dispersion coefficient can describe the mass decay inside the cavity over the whole ejection process.

REFERENCES

AHUJA, K. & MENDOSA, J. 1995 Effects of cavity dimensions, boundary layer and temperature on cavity noise with emphasis on benchmark data to validate computational aeroacoustics codes. *Final Report Contract NASA*-19061, Task 13. NASA Contractor Report.

ALVAREZ, J. O., KERSCHEN, E. J. & TUMIN, A. 2004 A theoretical model for cavity acustic resonances in subsonic flow. *AIAA Paper* 2004-2845.

BROWN, G. L. & ROSHKO, A. 1974 On density effects and large structure in turbulent mixing layers. *J. Fluid Mech.* **64**, 775–816.

DJENIDI, L., ELAVARASAN, R. & ANTONIA, R. A. 1999 The turbulent boundary layer over transverse square cavities. *J. Fluid Mech.* **395**, 271–294.

ETHEMBABAOGLU, S. 1973 On the fluctuating flow characteristics in the vicinity of gate slots. *Division of Hydraulic Engineering Report, University of Trondheim, Norwegian Institute of Technology.*

FORESTIER, N., JACQUIN, L. & GEFFROY, P. 2003 The mixing layer over a deep cavity at high subsonic speed. *J. Fluid Mech.* **475**, 101–145.

GLOERFELT, X., BOGEY, C., BAILLY, C. & JUVÉ, D. 2002 Aerodynamic noise induced by laminar and turbulent boundary layers over rectangular cavities. *AIAA Paper* 2002-2476.

GRACE, S. M., DEWAR, W. G. & WROBLEWSKI, D. E. 2004 Experimental investigation of the flow characteristics within a shallow wall cavity for both laminar and turbulent upstream boundary layers. *Exps. Fluids* **36**, 791–804.

HOWE, M. S. 1997 Edge, cavity and aperture tones at very low mach numbers. *J. Fluid Mech.* **330**, 61–84.

HUNT, J. C. R., WRAY, A. A. & MOIN, P. 1988 Eddies, stream, and convergence zones in turbulent flows. in *Proc. 1998 Summer Program*. pp. 193–208 Center for Turbulence Research, Stanford, CA, 1988.

KNISELY, C. & ROCKWELL, D. 1982 Self-sustained low frequency components in an impinging shear layer. *J. Fluid Mech.* **116**, 157–186.

Larchevêque, L., Sagaut, P., Mary, I., Labbé, O. & Comte, P. 2003 Large-eddy simulation of a compressible flow past a deep cavity. *Phys. Fluids* **15**, 193–210.

Larchevêque, L., Sagaut, P., Lê, T. H. & Comte, P. 2004 Large-eddy simulations of a compressible flow in a three-dimensional open cavity at high Reynolds number. *J. Fluid Mech.* **516**, 265–301.

Lin, J. C. & Rockwell, D. 2001 Organized oscillations of initially turbulent flow past a cavity. *AIAA J.* **39**, 1139–1151.

McCoy, A., Constantinescu, S. G. & Weber, L. 2005 LES simulation of contaminant removal from the embayment area between two vertical groynes in a channel. *XXXIst Intl Assoc. Hydraulic Research Congress, Seoul, Korea*.

Neary, M. D. & Stephanoff, K. D. 1987 Shear-layer-driven transition in a rectangular cavity. *Phys. Fluids* **30**, 2936–2946.

Pereira, J. C. F. & Sousa, J. M. M. 1994 Influence of impingement edge geometry on cavity flow oscillations. *AIAA J.* **32**, 1737–1740.

Pereira, J. C. F. & Sousa, J. M. M. 1995 Experimental and numerical investigation of flow oscillations in a rectangular cavity. *J. Fluids Engng* **117**, 68–73.

Pierce, C. D. & Moin, P. 2001 Progress-variable approach for large-eddy simulation of turbulent combustion. *Mech. Eng. Dept. Rep*. TF-80. Stanford University.

Rockwell, D. 1977 Prediction of oscillation frequencies for unstable flow past cavities. *J. Fluids Engng* **99**, 294–300.

Rockwell, D. & Knisely, C. 1980 Observation of the three-dimensional nature of unstable flow past a cavity. *Phys. Fluids* **23**, 425–431.

Rockwell, D. & Naudascher, E. 1978 Review-self-sustaining oscillations of flow past cavities. *J. Fluids Engng* **100**, 152–165.

Rossiter, J. E. 1964 Wind tunnel experiments on the flow over rectangular cavities at subsonic and transonic speeds. *Aero. Res. Counc. R&M* 3438.

Rowley, C. W., Colonius, T. & Basu, A. J. 2002 On self-sustained oscillations in two-dimensional compressible flow over rectangular cavities. *J. Fluid Mech.* **455**, 315–346.

Sarohia, V. 1977 Experimental investigation of oscillations in flows over shallow cavities. *AIAA J.* **15**, 984–991.

Shieh, C. M. & Morris, P. J. 2001 Comparison of two- and three-dimensional turbulent cavity flows. *AIAA Paper* 2001-0511.

Uijttewaal, W., Lehmann, D. & van Mazijk, A. 2001 Exchange processes between a river and its groyne fields: model experiments. *J. Hydraul. Engng* **127**, 928–936.

Yao, H., Cooper, R. K. & Raghunthan S. R. 2001 Large-eddy simulation of laminar-to-turbulent transition in incompressible flow past 3-D rectangular cavity. *AIAA Paper* 2001-31318.